

## ${}^6\text{H}$ states studied in the ${}^2\text{H}({}^8\text{He}, {}^4\text{He})$ reaction and evidence of an extremely correlated character of the ${}^5\text{H}$ ground state

E. Yu. Nikolskii,<sup>1,2,\*</sup> I. A. Muzalevskii,<sup>2,3</sup> A. A. Bezbakh,<sup>2,3</sup> V. Chudoba,<sup>2,3</sup> S. A. Krupko,<sup>2</sup> S. G. Belogurov,<sup>2,4</sup> D. Biare,<sup>2</sup> A. S. Fomichev,<sup>2,5</sup> E. M. Gazeeva,<sup>2</sup> A. V. Gorshkov,<sup>2</sup> L. V. Grigorenko,<sup>2,4,1</sup> G. Kaminski,<sup>2,6</sup> M. Khirk,<sup>7,2</sup> O. Kiselev,<sup>8</sup> D. A. Kostyleva,<sup>8,9</sup> M. Yu. Kozlov,<sup>10</sup> B. Mauey,<sup>2,11</sup> I. Mukha,<sup>8</sup> Yu. L. Parfenova,<sup>2</sup> W. Piatek,<sup>2,6</sup> A. M. Quynh,<sup>2,12</sup> V. N. Schetinin,<sup>10</sup> A. Serikov,<sup>2</sup> S. I. Sidorchuk,<sup>2</sup> P. G. Sharov,<sup>2,3</sup> N. B. Shulgina,<sup>1,13</sup> R. S. Slepnev,<sup>2</sup> S. V. Stepantsov,<sup>2</sup> A. Swiercz,<sup>2,14</sup> P. Szymkiewicz,<sup>2,14</sup> G. M. Ter-Akopian,<sup>2,5</sup> R. Wolski,<sup>2,15</sup> B. Zalewski,<sup>2,6</sup> and M. V. Zhukov<sup>16</sup>

<sup>1</sup>National Research Centre “Kurchatov Institute”, Kurchatov Square 1, 123182 Moscow, Russia

<sup>2</sup>Flerov Laboratory of Nuclear Reactions, JINR, 141980 Dubna, Russia

<sup>3</sup>Institute of Physics, Silesian University in Opava, 74601 Opava, Czech Republic

<sup>4</sup>National Research Nuclear University “MEPhI”, 115409 Moscow, Russia

<sup>5</sup>Dubna State University, 141982 Dubna, Russia

<sup>6</sup>Heavy Ion Laboratory, University of Warsaw, 02-093 Warsaw, Poland

<sup>7</sup>Skobeltsyn Institute of Nuclear Physics, Moscow State University, 119991 Moscow, Russia

<sup>8</sup>GSI Helmholtzzentrum für Schwerionenforschung GmbH, 64291 Darmstadt, Germany

<sup>9</sup>II. Physikalisches Institut, Justus-Liebig-Universität, 35392 Giessen, Germany

<sup>10</sup>Laboratory of Information Technologies, JINR, 141980 Dubna, Russia

<sup>11</sup>Institute of Nuclear Physics, 050032 Almaty, Kazakhstan

<sup>12</sup>Nuclear Research Institute, 670000 Dalat, Vietnam

<sup>13</sup>Bogoliubov Laboratory of Theoretical Physics, JINR, 141980 Dubna, Russia

<sup>14</sup>AGH University of Science and Technology, Faculty of Physics and Applied Computer Science, 30-059 Krakow, Poland

<sup>15</sup>Institute of Nuclear Physics PAN, Radzikowskiego 152, 31342 Kraków, Poland

<sup>16</sup>Department of Physics, Chalmers University of Technology, S-41296 Göteborg, Sweden



(Received 10 August 2021; revised 12 April 2022; accepted 26 May 2022; published 14 June 2022)

The extremely neutron-rich system  ${}^6\text{H}$  was studied in the direct  ${}^2\text{H}({}^8\text{He}, {}^4\text{He})$   ${}^6\text{H}$  transfer reaction with a 26A MeV secondary  ${}^8\text{He}$  beam. The measured missing mass spectrum shows a broad bump at  $\approx 4$ –8 MeV above the  ${}^3\text{H}+3n$  decay threshold. This bump can be interpreted as a broad resonant state in  ${}^6\text{H}$  at 6.8(5) MeV. The population cross section of such a presumably  $p$ -wave state (or it may be few overlapping states) in the energy range from 4 to 8 MeV is  $d\sigma/d\Omega_{\text{c.m.}} \simeq 190_{-80}^{+40} \mu\text{b/sr}$  in the angular range  $5^\circ < \theta_{\text{c.m.}} < 16^\circ$ . The obtained missing mass spectrum is practically free of  ${}^6\text{H}$  events below 3.5 MeV ( $d\sigma/d\Omega_{\text{c.m.}} \lesssim 5 \mu\text{b/sr}$  in the same angular range). The steep rise of the  ${}^6\text{H}$  missing mass spectrum at  $\approx 3$  MeV allows us to derive the lower limit for the possible resonant-state energy in  ${}^6\text{H}$  to be 4.5(3) MeV. According to the paring energy estimates, such a 4.5(3) MeV resonance is a realistic candidate for the  ${}^6\text{H}$  ground state (g.s.). The obtained results confirm that the decay mechanism of the  ${}^7\text{H}$  g.s. (located at 2.2 MeV above the  ${}^3\text{H}+4n$  threshold) is the “true” (or simultaneous)  $4n$  emission. The resonance energy profiles and the momentum distributions of fragments of the sequential  ${}^6\text{H} \rightarrow {}^5\text{H}(\text{g.s.})+n \rightarrow {}^3\text{H}+3n$  decay were analyzed by the theoretically updated direct four-body-decay and sequential-emission mechanisms. The measured momentum distributions of the  ${}^3\text{H}$  fragments in the  ${}^6\text{H}$  rest frame indicate very strong “dineutron-type” correlations in the  ${}^5\text{H}$  ground state decay.

DOI: [10.1103/PhysRevC.105.064605](https://doi.org/10.1103/PhysRevC.105.064605)

### I. INTRODUCTION

One of the important trends of modern experimental nuclear physics, taking advantage of radioactive ion beam techniques, is the expansion of our knowledge of nuclear systems located further beyond the proton and neutron drip lines. An important motivation here is the quest for the limits of nuclear structure existence: how far can we go beyond

the drip lines before coming to a situation in which resonant structures become completely “dissolved in continuum”?

Recently, reliable spectroscopic information was obtained on the extremely neutron-rich system  ${}^7\text{H}$  produced in the  ${}^2\text{H}({}^8\text{He}, {}^3\text{He})$   ${}^7\text{H}$  reaction [1,2]. The  ${}^6\text{H}$  population in the  ${}^2\text{H}({}^8\text{He}, {}^4\text{He})$   ${}^6\text{H}$  reaction, which is the subject of the present work, is a natural byproduct of the above-mentioned experiment.

Experimental information on the  ${}^6\text{H}$  resonant states is very limited. The authors of Ref. [3] reported a value  $E_T = 2.7(4)$  MeV (energy above the  ${}^3\text{H}+3n$  decay threshold) for the  ${}^6\text{H}$

\*enikolskii@mail.ru

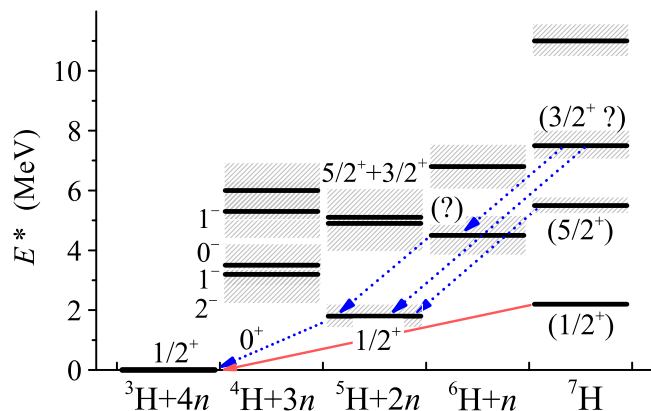


FIG. 1. The level schemes of  ${}^6\text{He}$ , and the known neighboring  ${}^4\text{He}$ ,  ${}^5\text{H}$  [9–11], and  ${}^7\text{H}$  [1,2] systems, which are important for the discussions of this work. The solid red arrow illustrates the decay mechanism of  ${}^7\text{H}$  g.s. which is expected to be “true”  $4n$  emission. The dotted blue arrows illustrate the decay mechanism of the higher excitations in  ${}^7\text{H}$ , which is expected to be the sequential  $2n + 2n$  and  $2n + n + n$  emissions via the  ${}^5\text{H}$  and  ${}^6\text{H}$  excited states, respectively.

state produced in the  ${}^7\text{Li}({}^7\text{Li}, {}^8\text{B}){}^6\text{H}$  reaction. This result was confirmed (with some reservations) in the  ${}^9\text{Be}({}^{11}\text{B}, {}^{14}\text{O}){}^6\text{H}$  reaction [4], giving  ${}^6\text{H}$  ground-state resonance energy  $E_T = 2.6(5)$  MeV. The search for  ${}^6\text{H}$  in the  ${}^6\text{Li}(\pi^-, \pi^+)$  reaction was carried out in [5,6]. No low-lying resonant states were identified, which led the authors to the conclusion that their results cast serious doubt on the existence of the  ${}^6\text{H}$  resonance in the 0–5 MeV unbound region. The observation of the  ${}^6\text{H}$  resonant states at  $E_T = \{6.6(7), 10.7(7), 15.3(7), 21.3(4)\}$  MeV, populated in the  ${}^9\text{Be}(\pi^-, pd){}^6\text{H}$  reaction, and  $E_T = \{7.3(10), 14.5(10), 22.0(10), 21.3(4)\}$  MeV states in the  ${}^{11}\text{B}(\pi^-, p^4\text{He}){}^6\text{H}$  reaction was reported in Ref. [7]. There was no indication of the resonant state at 2.6–2.9 MeV in this work. The  ${}^6\text{H}$  g.s. energy  $E_T = 2.9(9)$  MeV was determined in the  ${}^8\text{He}({}^{12}\text{C}, {}^{14}\text{N}){}^6\text{H}$  reaction [8]. Our results are in contradiction with [3,4,8] and are mostly in agreement with [5,7]. We demonstrate in this work that it is likely that the discussion about the actual position of the  ${}^6\text{H}$  g.s. is not finished yet, and it should be continued.

The search for the  ${}^6\text{H}$  resonant states is an exciting challenge in itself; however, here we face two important questions related also to our understanding of neighboring systems.

(i) What are the decay mechanisms of the  ${}^7\text{H}$  ground ( $E_T \approx 2.2$  MeV) and excited ( $E_T \approx 5.5$  MeV) states? This is defined by the spectra of its subsystems; see Fig. 1. For example, it could be either the true  ${}^7\text{H} \rightarrow {}^3\text{H} + 4n$  decay, or sequential  ${}^7\text{H} \rightarrow {}^5\text{H}(\text{g.s.}) + 2n$ , or  ${}^7\text{H} \rightarrow {}^6\text{H}(\text{g.s.}) + n$  decay, depending on the ground state energies of  ${}^5\text{H}$  and  ${}^6\text{H}$ . While for  ${}^4\text{H}$  and  ${}^5\text{H}$  there are some relatively reliable data, the spectrum of  ${}^6\text{H}$  is very uncertain.

(ii) What is the decay mechanism of the  ${}^6\text{H}$  ground state? An intuitive view of the situation, also confirmed by the theoretical estimates of this work, tells us that the  ${}^6\text{H}$  g.s. decay is likely to have a sequential  ${}^6\text{H} \rightarrow {}^5\text{H}(\text{g.s.}) + n \rightarrow {}^3\text{H} + 3n$  character. Therefore, by studying the  ${}^6\text{H}$  decay, we may also gain access to the decay properties of the  ${}^5\text{H}$  ground state. The

momentum distributions of the  ${}^3\text{H}$  fragment, measured in our experiment, can be interpreted by assuming an unexpectedly strong “dineutron” correlation character of the  ${}^5\text{H}$  ground state decay. The sequential  ${}^6\text{H} \rightarrow {}^5\text{H}(\text{g.s.}) + n \rightarrow {}^3\text{H} + 3n$  decay has never been studied before, and interpretation of the data required extensive model studies and discussions of this decay mechanism. Our results highlight the potential of the sequential  ${}^6\text{H} \rightarrow {}^5\text{H}(\text{g.s.}) + n \rightarrow {}^3\text{H} + 3n$  decay as an important source of information about the intermediate  ${}^5\text{H}$  system.

The data of this work obtained in the double  ${}^4\text{He} - {}^3\text{H}$  coincidences have quite large statistics (among available data only for the  ${}^9\text{Be}(\pi^-, pd){}^6\text{H}$  reaction [7] is statistics better), and it allows for a good missing mass (MM) energy resolution for the  ${}^6\text{H}$  spectrum and careful treatment of the backgrounds. The consistent MM picture was obtained in the triple  ${}^4\text{He} - {}^3\text{H} - n$  coincidence data, which provide much smaller statistical confidence, but which can be seen as practically background free. Thus, the detailed information on the low-energy spectrum of  ${}^6\text{H}$  derived from our data sheds light on the above-mentioned problems.

## II. EXPERIMENT

The experiment was performed in the Flerov Laboratory of Nuclear Reactions (JINR, Dubna) at the recently commissioned ACCULINNA-2 fragment-separator coupled to the U-400M heavy ion cyclotron [12]. Recently  ${}^7\text{H}$  studies were carried out in the  ${}^2\text{H}({}^8\text{He}, {}^3\text{He}){}^7\text{H}$  reaction [1,2]. The information on  ${}^6\text{H}$  is naturally present in the data of these experiments due to a “satellite”  ${}^2\text{H}({}^8\text{He}, {}^4\text{He}){}^6\text{H}$  reaction. The  ${}^7\text{H}$  experiments were discussed in detail in Ref. [2], and we only briefly sketch here the information important for understanding the  ${}^6\text{H}$  data.

The  ${}^6\text{H}$  system was produced in the  ${}^2\text{H}({}^8\text{He}, {}^4\text{He}){}^6\text{H}$  reaction. The secondary  ${}^8\text{He}$  beam was produced by the 33.4A MeV  ${}^{11}\text{B}$  primary beam fragmentation on a 1 mm Be target. The  ${}^8\text{He}$  beam with intensity of  $\approx 10^5$  pps at 26A MeV and  $\approx 90\%$  beam purity interacted with the deuterium nuclei in the cryogenic gas target; see Fig. 2. The target was 4 mm thick with  $6\ \mu\text{m}$  thick entrance and exit stainless steel windows. Being cooled down to 27 K, it had a thickness of  $3.7 \times 10^{20}\text{cm}^{-2}$ . The secondary beam diagnostics, made with a pair of thin time-of-flight (ToF) plastics and a pair of position-sensitive chambers [13], provided the determination of the hit position on the target and the time-of flight measurement made for every individual beam ion with accuracy 1.8 mm and 280 ps, respectively.

The experimental setup, discussed in detail in Ref. [2], involved four “sideways”  $\Delta E$ - $E$ - $E$  telescopes detecting the recoil nuclei ( ${}^4\text{He}$  in this experiment) emitted from the cryogenic deuterium gas target in the angular range  $8^\circ$ – $26^\circ$  in the laboratory system. A  $20\ \mu\text{m}$  thick,  $50 \times 50\ \text{mm}^2$  single-sided Si front detector of the telescope had 16 strips. Next to this  $\Delta E$  detector was a 1 mm thick,  $61 \times 61\ \text{mm}^2$  double-sided Si strip detector having behind it another 1 mm thick veto detector. The “central” telescope, assigned for the registration of the  ${}^3\text{H}$  fragments, originating from the  ${}^6\text{H}$  decay, consisted of a 1.5 mm thick  $64 \times 64\ \text{mm}^2$  double-sided Si strip detector followed by a  $4 \times 4$  array of CsI(Tl) scintillators. The charged

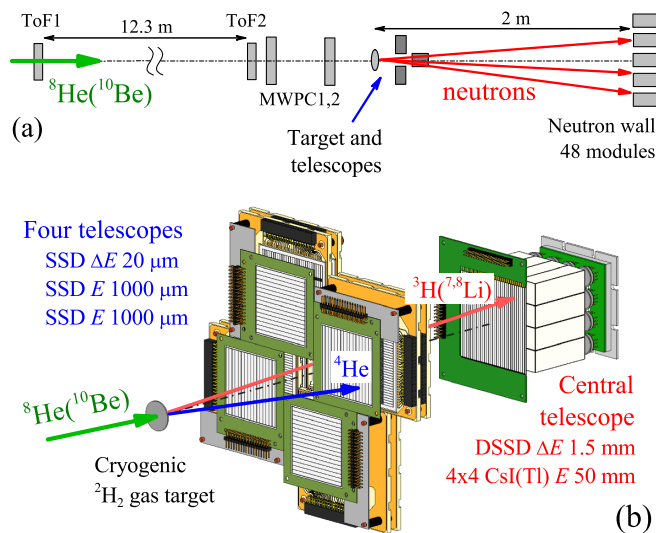


FIG. 2. Experimental setup for the  ${}^2\text{H}({}^8\text{He}, {}^4\text{He}){}^6\text{H}$  and  ${}^2\text{H}({}^{10}\text{Be}, {}^4\text{He}){}^8\text{Li}$  reactions study: (a) general view and (b) target and charged particle telescopes assembly.

particles, namely the “fast” decay tritons (with laboratory energy  $\approx 70 \pm 30$  MeV) or Li isotopes [in the case of the reference  ${}^2\text{H}({}^{10}\text{Be}, {}^4\text{He}){}^8\text{Li}^*$  reaction], were registered in the narrow forward cone  $\theta \leq 6^\circ$ , with good angular ( $\Delta\theta \leq 0.5^\circ$ ) and energy ( $\Delta E/E \leq 2\%$ ) resolutions.

The typical identification (ID) plots obtained with these detector telescopes are illustrated in Fig. 3. A good quality of the helium isotopes’ identification is found; see panel (a), where the green dots show the coincidences with “fast” tritons as well. The central telescope performance is illustrated in Fig. 3(b), giving as an example the  ${}^2\text{H}({}^{10}\text{Be}, {}^4\text{He}){}^8\text{Li}$  calibration reaction study. All hydrogen and lithium isotopes are obviously well separated here.

The setup also included a neutron wall consisting of 48 stilbene-crystal modules where each 50 mm thick crystal was 80 mm in diameter [14]. The neutron wall was located near zero angle at a  $\approx 2$  m distance from the deuterium target; see Fig. 2(a). The neutron spectrometer involved into the triple  ${}^4\text{He}-{}^3\text{H}-n$  coincidences has a good  $n-\gamma$  separation, provided by the so-called pulse-shape analysis method [14]; see Fig. 4.

A dedicated measurement with the 42A MeV secondary  ${}^{10}\text{Be}$  beam (produced from the 50A MeV  ${}^{15}\text{N}$  primary beam) was performed to provide independent calibration of the setup; see Sec. II B.

### A. The Monte Carlo simulations

Complete Monte Carlo (MC) simulations of the experimental setup for the  ${}^2\text{H}({}^8\text{He}, {}^4\text{He}){}^6\text{H}$  reaction were performed. The  ${}^6\text{H}$  MM resolution of the experiment,  $\approx 0.8\text{--}1.7$  MeV, was determined in different kinematical ranges; see Table I for details. The maximum efficiencies (at  $E_T \approx 5\text{--}7$  MeV) of the double  ${}^4\text{He}-{}^3\text{H}$  and triple  ${}^4\text{He}-{}^3\text{H}-n$  coincidence detections were  $\approx 65\%$  and  $\approx 4\%$ , respectively. The setup efficiency as a function of MM and the reaction center-

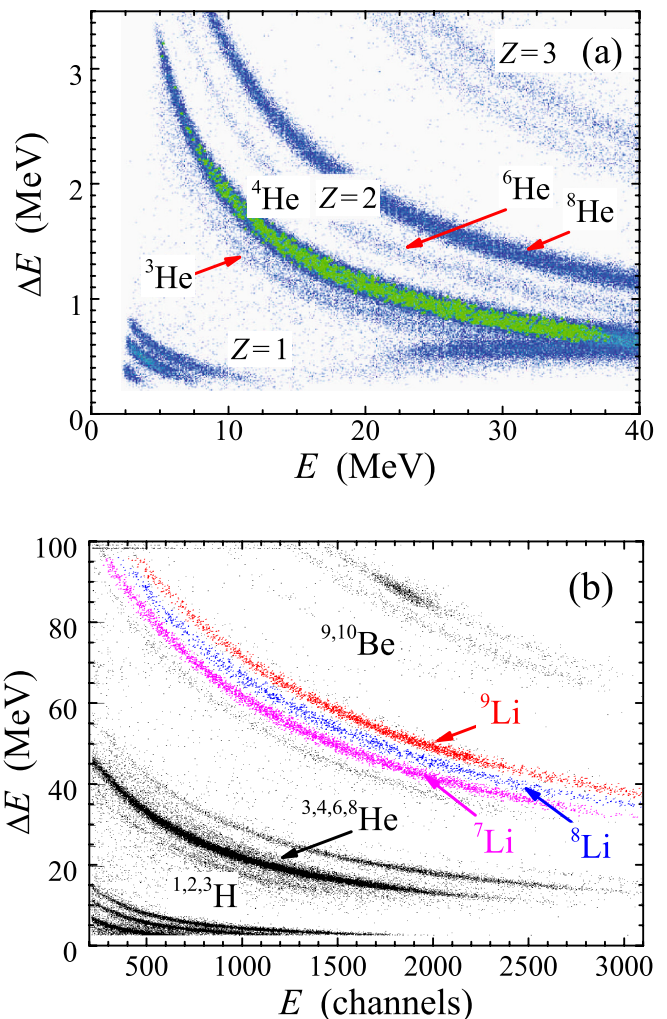


FIG. 3. Typical ID plots. (a) For the sideways telescopes in the  ${}^2\text{H}({}^8\text{He}, {}^4\text{He}){}^6\text{H}$  reaction, where the green dots show the  ${}^4\text{He}-{}^3\text{H}$  coincidences forming the  ${}^6\text{H}$  spectrum. (b) For the central telescope in the  ${}^2\text{H}({}^{10}\text{Be}, {}^4\text{He}){}^8\text{Li}$  reaction assigned to calibration of the  ${}^6\text{H}$  MM spectrum.

of-mass angle,  $\theta_{\text{c.m.}}$ , is demonstrated in Fig. 12(a). Important qualitative results of these studies are the following.

(i) In the MM energy range of interest,  $E_T \approx 3\text{--}10$  MeV, the setup efficiency is both high and monotonic. The largest variation of efficiency is quite modest, e.g.,  $\approx 40\%$ .

TABLE I. The  ${}^6\text{H}$  MM energy resolution (in MeV) of the setup for the  ${}^2\text{H}({}^8\text{He}, {}^4\text{He}){}^6\text{H}$  reaction according to MC simulations. The resolution is shown as function of the  ${}^6\text{H}$  MM energy (columns, in MeV) and center-of-mass reaction angle (rows, in degrees). Missing values correspond to a near zero efficiency of the setup.

| $\theta_{\text{c.m.}}$ | 5   | 10  | 15  | 20  |
|------------------------|-----|-----|-----|-----|
| $10^\circ$             | 1.7 | 1.3 | 1.0 | 0.8 |
| $20^\circ$             | 1.7 | 1.5 | 1.3 | 1.0 |
| $30^\circ$             |     |     | 1.4 | 1.2 |

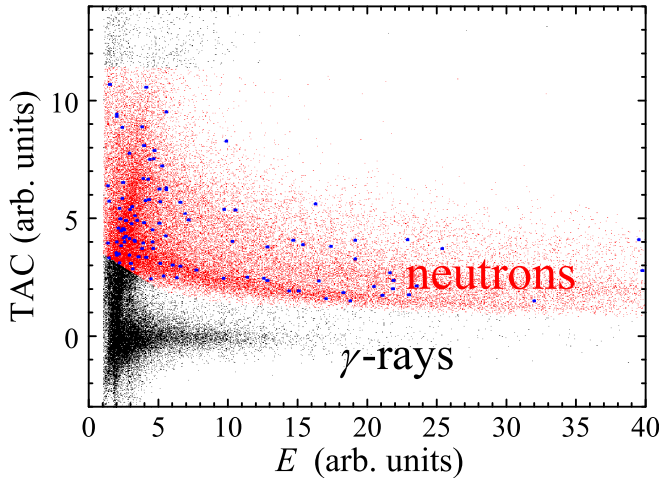


FIG. 4. The ID plot for neutron spectrometer (time-to-amplitude ID parameter vs neutron energy). Red dots show events identified as neutrons and blue dots indicate such events involved in triple  ${}^4\text{He}$ - ${}^3\text{H}$ - $n$  coincidences.

(ii) At about  $\theta_{\text{c.m.}} \approx 16^\circ$  the setup efficiency abruptly drops. Therefore, the data interpretation for  $\theta_{\text{c.m.}} > 16^\circ$  becomes problematic due to the high sensitivity to details of possible efficiency correction procedures.

Detailed MC simulations of the theoretically motivated  ${}^6\text{H}$  MM spectra (see Fig. 12) and the isolated  ${}^6\text{H}$  resonance, expected according to Refs. [3,4,8] at  $E_T \approx 2.6$  MeV (see Fig. 13), were performed, as were MC studies of the calibration  ${}^2\text{H}({}^{10}\text{Be}, {}^4\text{He}){}^8\text{Li}$  reaction (see Fig. 5).

### B. The neutron-unstable ${}^8\text{Li}$ spectrum populated in the ${}^2\text{H}({}^{10}\text{Be}, {}^4\text{He}){}^8\text{Li}$ reaction

A dedicated test experiment was performed with the  ${}^{10}\text{Be}$  beam for the setup calibration. The known neutron-unstable  ${}^8\text{Li}$  states were populated in the  ${}^2\text{H}({}^{10}\text{Be}, {}^4\text{He}){}^8\text{Li}$  reaction. The  $\Delta E$ - $E$  plots viewed in the case where the 42A MeV  ${}^{10}\text{Be}$

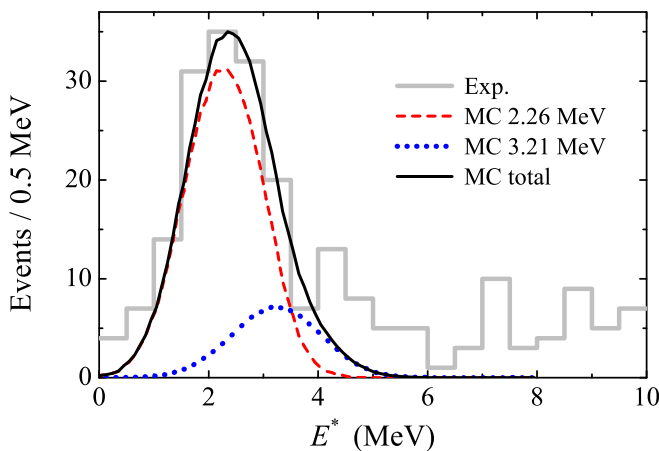


FIG. 5. The  ${}^8\text{Li}$  spectrum obtained in the  ${}^2\text{H}({}^{10}\text{Be}, {}^4\text{He}){}^8\text{Li}^*$  reaction for  ${}^4\text{He}$ - ${}^7\text{Li}$  coincidence events.

nuclei bombarded the deuterium gas target were even more filled in their  ${}^4\text{He}$  loci than in the case of the  ${}^8\text{He}$  projectiles. However, by imposing the  ${}^4\text{He}$ - ${}^8\text{Li}$  coincidence condition this background was strongly reduced. The first two particle-stable states of  ${}^8\text{Li}$  (corresponding to the  ${}^4\text{He}$ - ${}^8\text{Li}$  coincidence events) were found to be poorly populated in this reaction. The first neutron-unstable resonant state, known to be at the excitation energy of  $E^* = 2.26$  MeV [15], is well seen in the  ${}^4\text{He}$ - ${}^7\text{Li}$  coincidence events in Fig. 5. The energy of this state is measured with 250 keV error, but also is well interpreted by assuming that the next  ${}^8\text{Li}$  state with  $E^* = 3.21$  MeV is populated with relative  $\approx 30\%$  probability, as predicted in the FRESKO calculations.

### III. THE ${}^6\text{H}$ DATA

The  ${}^4\text{He}$ - ${}^3\text{H}$  coincidence data (4650 events in total) obtained in the  ${}^2\text{H}({}^8\text{He}, {}^4\text{He}){}^6\text{H}$  reaction are shown in Fig. 6. The setup of experiment [2] was optimized for the  ${}^7\text{H}$  search in the  ${}^2\text{H}({}^8\text{He}, {}^3\text{He}){}^7\text{H}$  reaction, and, therefore, it was not optimal for the  ${}^6\text{H}$  studies. For that reason a relatively narrow center-of-mass (c.m.) angular range was available for the  ${}^4\text{He}$  recoils originating from the  ${}^2\text{H}({}^8\text{He}, {}^4\text{He}){}^6\text{H}$  reaction; see Fig. 6(b). Background conditions were quite poor for these recoils because of random coincidences with  $\alpha$ 's originating from other intense reaction channels. This background can be seen in Fig. 6(a) as the strong population of the  $\{E_T, E_{3\text{H}}\}$  plane beyond the kinematical limit for the  ${}^2\text{H}({}^8\text{He}, {}^4\text{He}){}^6\text{H}$  reaction ( $E_{3\text{H}}$  is the  ${}^3\text{H}$  energy in the  ${}^6\text{H}$  c.m. frame). The background in the low-energy part of the MM spectrum can be drastically reduced by gating the data in the kinematically allowed range  $E_{3\text{H}} < E_T/2$  on the  $\{E_T, E_{3\text{H}}\}$  plane. This selection results in 3850 events shown by red dots in Fig. 6(b). The  ${}^6\text{H}$  MM spectrum derived from these events [blue histogram in Fig. 6(c)] shows a rise in the region beginning at  $E_T = 3.0$ – $3.5$  MeV and going up to  $E_T = 6$  MeV, where the spectrum remains flat within the energy range extending up to  $E_T = 9$  MeV. The rate of this rise, coming to the flat top, matches well the shape characteristic for relatively broad  $p$ -wave resonant states, as can be expected for  ${}^6\text{H}$ . This rate is much faster than one may expect in a situation without resonant contributions [for example, the four-body phase volume case is illustrated by the orange dotted curve in Fig. 6(c)]. This specific shape of the MM spectrum allows us to claim that there is a resonance state or a group of overlapping resonance states in  ${}^6\text{H}$  located at MM energy  $E_T \approx 6.8$  MeV.

The 6.8 MeV bump can be made more visible by limiting the reaction c.m. angular range as  $\theta_{\text{c.m.}} < 16^\circ$ ; see the gray histogram in Fig. 6(c). All the MM spectra gated by some  $\theta_{\text{c.m.}}$  bands with  $\theta_{\text{c.m.}} > 16^\circ$  show no resonating behavior, only monotonic growth up to  $E_T \approx 20$  MeV [for example, see the red histogram in Fig. 6(c)]. Partly this is due to the setup efficiency in the  $E_T \approx 6.8$  MeV energy range, which rapidly degrades at  $\theta_{\text{c.m.}} \gtrsim 16^\circ$  and comes to zero at  $\theta_{\text{c.m.}} \approx 22^\circ$ . In contrast, the energy range  $E_T \gtrsim 10$ – $15$  MeV for  $\theta_{\text{c.m.}} > 16^\circ$  is strongly boosted due to the setup geometry. This effect is well illustrated in Figs. 6(b) and 12(a).

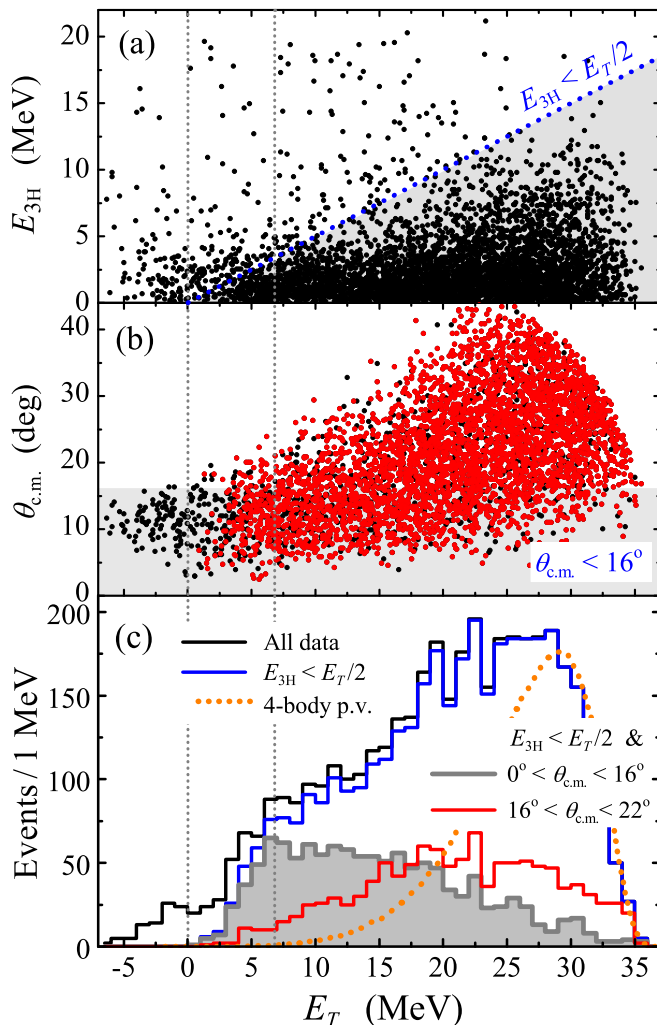


FIG. 6. Data on the  ${}^4\text{He}$ - ${}^3\text{H}$  coincidence events considered for the ascertainment of the  ${}^6\text{H}$  MM energy spectrum. (a) Correlation between the  ${}^3\text{H}$  energy in the  ${}^6\text{H}$  c.m. frame  $E_{3\text{H}}$  and the  ${}^6\text{H}$  MM energy  $E_T$ . The gray triangle, bounded by the blue dotted line, shows the kinematically allowed region. (b) Correlation between the center-of-mass reaction angle and the  ${}^6\text{H}$  MM energy. The gray rectangle shows the  $\theta_{\text{c.m.}} < 16^\circ$  cutoff region. (c) The  ${}^6\text{H}$  missing mass spectra: complete data (black histogram), kinematical cutoff  $E_{3\text{H}} < E_T/2$  (blue histogram), and additional cutoffs  $\theta_{\text{c.m.}} < 16^\circ$  (filled gray histogram) and  $16^\circ < \theta_{\text{c.m.}} < 22^\circ$  (red histogram). The orange dotted curve illustrates the four-body phase volume  $\approx E_T^{7/2}$  convoluted with the setup bias. The vertical gray dotted lines indicate the  ${}^3\text{H} + 3n$  threshold and the position of the 6.8 MeV  ${}^6\text{H}$  resonant state.

### A. The ${}^6\text{H}$ c.m. angular distribution

The cross section of the  ${}^2\text{H}({}^8\text{He}, {}^4\text{He}){}^6\text{H}$  reaction populating the expected low-lying resonant states of  ${}^6\text{H}$  was calculated using the FRESKO code for  $\Delta l = 1$  momentum transfer. The calculations are analogous to those performed in [2] for the  ${}^2\text{H}({}^8\text{He}, {}^3\text{He}){}^7\text{H}$  reaction with the “standard” parameter set. The obtained center-of-mass cross section is shown in Fig. 7. The cross section features a broad peak at about  $\theta_{\text{c.m.}} \approx 8^\circ$ , rapid fall after  $\theta_{\text{c.m.}} > 14$ – $16^\circ$ , and the diffraction minimum around  $\theta_{\text{c.m.}} \approx 24^\circ$ .

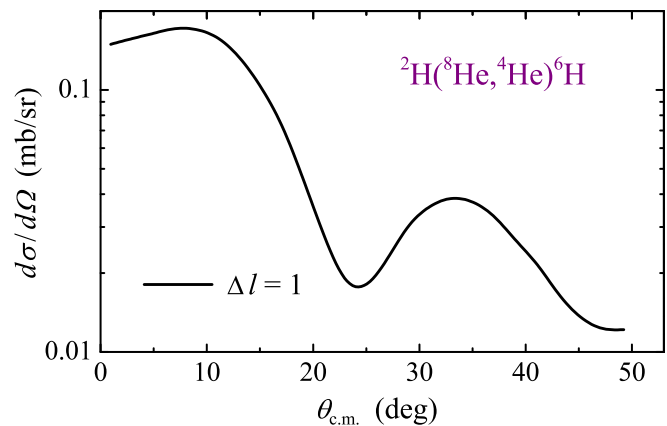


FIG. 7. The  $\Delta l = 1$  cross section for the  ${}^2\text{H}({}^8\text{He}, {}^4\text{He}){}^6\text{H}$  reaction obtained in FRESKO calculations.

In paper [2] the “standard” parameter set for FRESKO calculations was modified to explain the experimentally observed missing population in the angular range  $10^\circ < \theta_{\text{c.m.}} < 14^\circ$ , which was assumed to correspond to the diffraction minimum of the  ${}^2\text{H}({}^8\text{He}, {}^3\text{He}){}^7\text{H}$  reaction. The “standard” parameter set predicted this diffraction minimum at  $\theta_{\text{c.m.}} \approx 18^\circ$ . Strong absorption or extreme peripheral character of the reaction were suggested in [2] to explain the low-angle shift of the diffraction minimum. One may expect that such a parameter modification is needed also for the  ${}^2\text{H}({}^8\text{He}, {}^4\text{He}){}^6\text{H}$  reaction calculations. However, both (i) the situation observed in Fig. 7 with diffraction minimum at about  $\theta_{\text{c.m.}} \approx 24^\circ$  and (ii) the hypothetic situation of the diffraction minimum shifted to smaller c.m. angles are qualitatively consistent with the absence of the 6.8 MeV bump in the experimental MM spectrum for  $\theta_{\text{c.m.}} > 16^\circ$  observed in Fig. 6(c); the angular range  $16^\circ < \theta_{\text{c.m.}} < 22^\circ$  may correspond either to the diffraction minimum for the  $\Delta l = 1$  cross section or to the right slope of its low-angle forward peak.

### B. “Direct” empty target subtraction

The background contribution can be further reduced by taking into account the empty target (deuterium gas out) data; see Fig. 8. The empty target measurement collected around 17% of the beam integral providing 280 events in total and 190 events within the “energy triangle” of Fig. 8(a).

We first use two simple procedures of the “direct” background subtraction of the scaled empty target data. In the first case the total spectra are the subject of subtraction; see Fig. 8(c), black diamonds. Alternatively, the empty target spectrum is subtracted in the kinematical limits  $E_{3\text{H}} < E_T/2$  and  $\theta_{\text{c.m.}} < 16^\circ$  (gray circles). Two features should be pointed out here:

(i) The subtraction spectra in the energy range 3.5–10 MeV are consistent with each other and consistent with the 6.8 MeV bump position as seen in the spectrum without any background subtraction.

(ii) In both cases we get quite a low limit for the population of the  $E_T = 0$ – $3.5$  MeV energy range (the corresponding

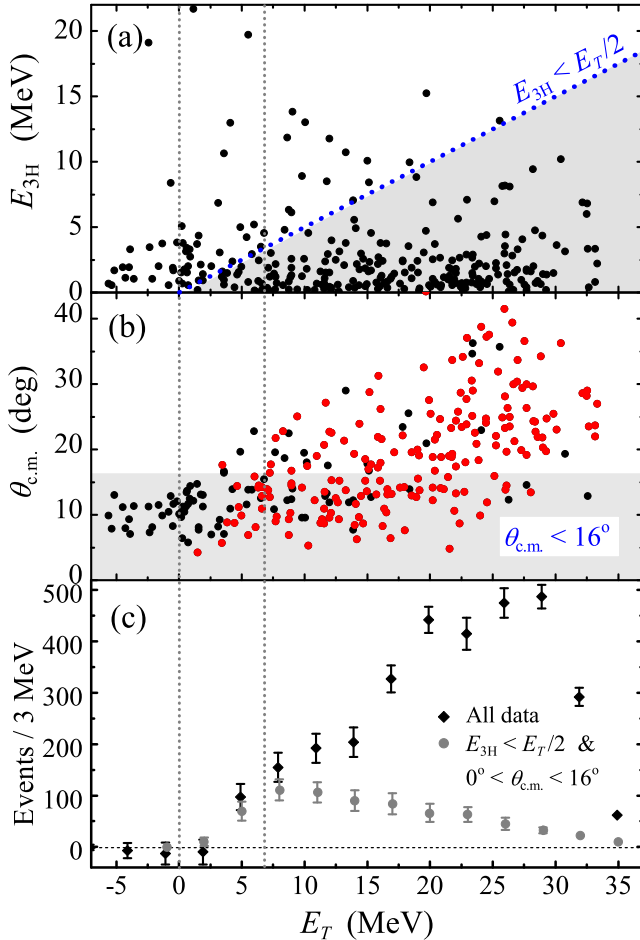


FIG. 8. Empty target data for the  $^4\text{He}$ - $^3\text{H}$  coincidence events (see Fig. 6 caption for more details) and background subtracted  $^6\text{H}$  spectra (direct subtraction). (a) Correlation between the  $^3\text{H}$  energy in the  $^6\text{H}$  c.m. frame  $E_{3H}$  and the  $^6\text{H}$  MM energy  $E_T$ . (b) Correlation between the center-of-mass reaction angle and the  $^6\text{H}$  MM energy. (c) The  $^6\text{H}$  MM spectrum after scaled empty target data subtraction: complete data (black diamonds), kinematical cutoff  $E_{3H} < E_T/2$ , and  $\theta_{c.m.} < 16^\circ$  (gray circles).

limits are  $0 \pm 25$  events and  $10 \pm 9$  events). This point also is further discussed in Sec. V A.

So, both direct subtraction methods produce consistent results and indicate that we understand the nature of the apparatus-induced backgrounds in our experiment. However, because of the low statistics of the empty target data the  $E_T$  bin size was to be set to quite a large value of 3 MeV. Despite the large bin size, the statistical error bars produced by the two used procedures are quite large and do not allow detailed quantitative conclusions. For that reason a more stable background subtraction procedure is developed, which is based on the smooth approximation of the empty target background data.

### C. “Advanced” empty target subtraction

This subtraction procedure is based on assumption that the empty target contribution is sufficiently smooth in the

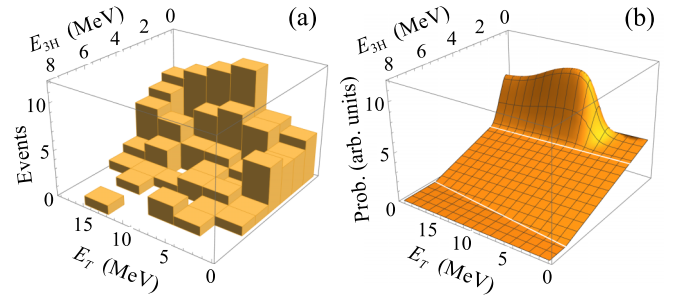


FIG. 9. (a) Empty target data in the correlation plane  $\{E_T, E_{3H}\}$ . (b) Empty target data fit by a smooth analytical function.

kinematical space. The empty target data histogram in the  $\{E_T, E_{3H}\}$  plane is shown in Fig. 9(a). This background has two components: the flat component, weakly depending on energy, and the relatively narrow “ridge” at small  $E_{3H}$  values. It was approximated by a smooth analytical function—see Fig. 9(b)—and then a MC procedure was used to subtract it from the data. The subtraction results obtained with the empty-target data normalized to the  $^8\text{He}$  incoming beam flux are shown in Fig. 10. The motivation for the use of complicated “two-dimensional” background subtraction procedure and important conclusions obtained as a result of this procedure are emphasized by the following two issues.

(i) One may see in Figs. 10(c) and 10(d) that the subtraction procedure reduces to zero the contributions in the kinematically forbidden ranges  $\varepsilon = 2E_{3H}/E_T > 1$  for the MM ranges  $\{3.5, 5.5\}$  and  $\{5.5, 7.5\}$ . This is a good indication that the background subtraction procedure is reasonably well “calibrated” for the energy region of interest.

(ii) The energy distribution in Fig. 10(b) is flat, and there is no considerable event concentration in the kinematically allowed range  $\varepsilon < 1$ . If there is a flat background distribution in the  $\{E_T, E_{3H}\}$  plane for  $E_T < 3$  MeV, then, evidently, the corresponding background contribution to the MM spectrum with the physical kinematical selection  $E_{3H} < E_T/2$  should be linear at  $E_T < 3$ . This is actually taking place, and, as a result, the whole  $^6\text{H}$  spectrum is effectively reduced to zero in the MM range  $E_T < 3$  MeV; see Fig. 10(a).

The 6.8 MeV bump is clearly seen in the empty-target-corrected MM spectrum in Fig. 10(a), with an average cross section of  $\simeq 190(40)\mu\text{b}/\text{sr}$  being deduced for the c.m. angular range  $5^\circ < \theta_{c.m.} < 16^\circ$ . This reasonably large cross section is consistent with the resonant population mechanism. This value is also in a very good agreement with the cross section obtained by FRESKO calculations; see Fig. 7. The steep rise of the spectrum at 3.0–3.5 MeV and the broad left tail of the 6.8 MeV bump provide together an indication that another  $^6\text{H}$  state may be located at about 4.5 MeV; see the discussion of Figs. 12(c) and 12(d) in Sec. III E below. No indication of the 2.6–2.9 MeV state (the  $^6\text{H}$  ground state, as suggested in Refs. [3,4,8]) is found.

### D. Neutron coincidence data

Practically background-free  $^6\text{H}$  data can be obtained by requiring coincidence with one of the neutrons emitted in

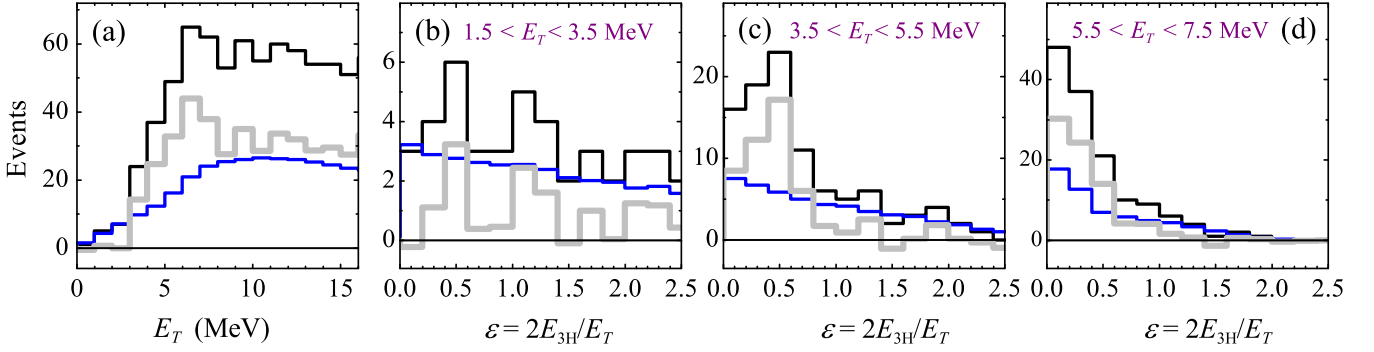


FIG. 10. Advanced empty target background subtraction. Initial  ${}^6\text{H}$  data [black histogram; see gray histogram in Fig. 6(c)], scaled background (blue histogram), and corrected data (gray histogram). Panel (a) shows the  ${}^6\text{H}$  MM spectrum. Panels (b), (c), and (d) show the  $\epsilon$  distributions of the  ${}^3\text{H}$  fragment in the  ${}^6\text{H}$  rest frame obtained in the MM  $E_T$  ranges  $\{1.5, 3.5\}$ ,  $\{3.5, 5.5\}$ , and  $\{5.5, 7.5\}$  MeV, respectively.

the  ${}^6\text{H}$  decay. The data on the  ${}^4\text{He}-{}^3\text{H}-n$  coincidence events (130 in total) from the  ${}^2\text{H}({}^8\text{He}, {}^4\text{He}){}^6\text{H}$  reaction are shown in Fig. 11. The background level of this spectrum can be estimated as  $\lesssim 3\%$  from the “kinematical triangles” built for the  ${}^3\text{H}$  and neutron emitted by  ${}^6\text{H}$ ; see Figs. 11(a) and 11(b). The c.m. angular distribution of the  ${}^4\text{He}-{}^3\text{H}-n$  coincidence events is shown in Fig. 11(c). There is evidence that there is a peak at 6.8 MeV in Fig. 11(d), where indication on the 4.5 MeV structure can be also found. There is no evidence of the possible 2.6 MeV state in Fig. 11: just one event is found in the 1.5 MeV energy bin around  $E_T = 2.6$  MeV compared to the total 14 events within the  $E_T \approx 3\text{--}8$  MeV MM energy range, assigned to the broad 6.8 MeV peak.

It is important to note that the neutron coincidence MM spectrum is nicely described by the same curves as the empty-target-subtracted MM spectrum; see Fig. 12. This statement is, of course, valid within the much larger statistical uncertainty of the neutron coincidence data.

### E. ${}^6\text{H}$ spectrum interpretation

It should be carefully specified why and in which sense we speculate above about the 6.8 MeV state (and, moreover, about the 4.5 MeV state).

Possible interpretations of the low-energy  ${}^6\text{H}$  spectrum are illustrated in Fig. 12. In this figure the empty-target-corrected  ${}^4\text{He}-{}^3\text{H}$  coincidence spectrum of Fig. 10(a) and the  ${}^4\text{He}-{}^3\text{H}-n$  coincidence spectrum of Fig. 11(d) are also corrected for the experimental efficiency by a MC procedure. For consistency, the neutron coincidence spectrum in Fig. 12(d) has the same  $\theta_{\text{c.m.}} < 16^\circ$  cutoff.

The four-body  ${}^3\text{H}+n+n+n$  and two-body  ${}^5\text{H}+n$  phase volumes (orange dotted curves) illustrate the possible profiles of nonresonant “physical backgrounds” in Figs. 12(b) and 12(c). We may see that such “standard” backgrounds have profiles which cannot explain the strong population of the  $E_T \approx 3\text{--}8$  MeV MM range. Some resonant contributions are also needed.

The resonant cross section behavior at  $E_T < 9$  MeV is approximated by the conventional Lorentz-like profiles

$$\frac{d\sigma}{dE_T} \approx \frac{\Gamma(E_T)}{(E_r - E_T)^2 + \Gamma(E_T)^2/4},$$

“corrected” for the energy dependence of the width defined by Eq. (3) below.

The interpretation with a single broad resonant peak is given in Fig. 12(b); see the black solid curve. In these estimates we use the width  $\Gamma = 5.5$  MeV for the  $E_T = 6.8$  MeV resonant state; see Fig. 16. This width value is likely to be the upper limit for the  ${}^6\text{H}$  resonant state, because the upper-limit parameters are used in the estimates. For example, the maximum single-particle reduced width  $\theta^2 = 1.5$  is used in Eq. (4) for the  ${}^5\text{H}-n$  channel. For this interpretation there is some indication of underestimation of the spectrum in the low-energy region  $E_T = 3\text{--}5$  MeV. For a *smaller* width of the  $E_T = 6.8$  MeV resonant state or for a *higher resonant energy* selection, this underestimation becomes larger and is regarded as not acceptable.

Statistically, the valley in the experimental spectrum around  $E_T = 8\text{--}10$  MeV may be regarded as not very significant. The “smooth” description of the data without an explicit resonant bump [see Fig. 12(b), black dashed curve] has a  $\chi^2$  value only somewhat larger than unity. This is much worse than in the “broad peak” interpretation [black solid curve in Fig. 12(b)], but statistically this is an acceptable value for the  $\chi^2$  criterion. However, for such a “smooth” fit we still need a resonant state at  $E_T = 6.8$  MeV. For the “smooth” description of the data also the resonance energy values  $E_T < 6.8$  MeV are acceptable. However, higher resonance energy values  $E_T > 6.8$  MeV are not acceptable due to the systematic underestimation of the low-energy data. Thus, the  $E_T = 6.8$  MeV resonance energy can be regarded as an *upper limit resonant energy* admissible for the data interpretation with a *single broad state*.

One may find in Figs. 12(b), 12(c) that for the  ${}^6\text{H}$  MM spectrum in the  $E_T = 4\text{--}8$  MeV energy range up to  $\approx 35\%$  of the population cross section can be related to “physical background” connected with low-energy tail of the higher excitations. For that reason the lower limit given for the uncertainty of the population cross section should be extended as  $d\sigma/d\Omega_{\text{c.m.}} \simeq 190_{-80}^{+40} \mu\text{b/sr}$ .

### F. Where is the ${}^6\text{H}$ ground state?

An important feature of our data is the nonobservation of the  ${}^6\text{H}$  ground state at  $E_T = 2.6\text{--}2.9$  MeV, as proposed in the

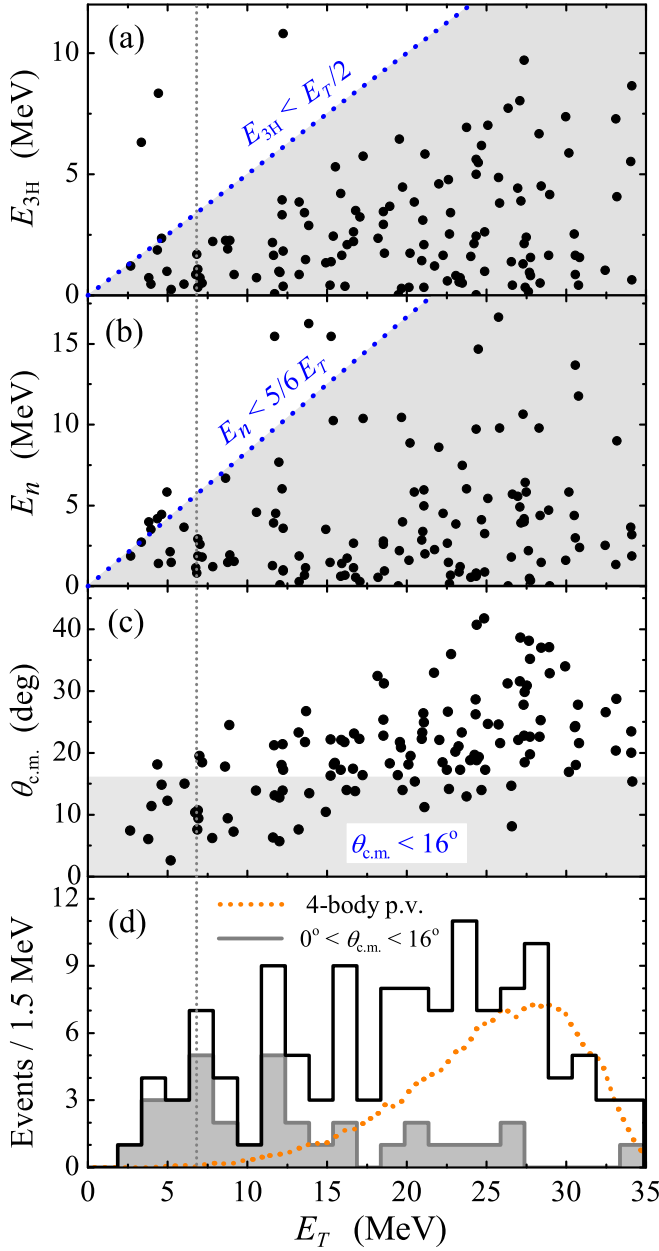


FIG. 11. The  ${}^4\text{He}-{}^3\text{H}-n$  coincidence events. (a) Correlation between the  ${}^3\text{H}$  energy in the  ${}^6\text{H}$  c.m. frame and the  ${}^6\text{H}$  MM energy. (b) Correlation between the neutron energy in the  ${}^6\text{H}$  c.m. frame and the  ${}^6\text{H}$  MM energy. The gray triangles in (a) and (b) show the kinematically allowed regions. (c) Correlation between the center-of-mass reaction angle and the  ${}^6\text{H}$  MM energy. The gray rectangle shows the  $\theta_{\text{c.m.}} < 16^\circ$  cutoff region. (d) The  ${}^6\text{H}$  missing mass spectrum gated by the kinematically allowed region of panel (a). The vertical gray dotted line indicates the position of the 6.8 MeV  ${}^6\text{H}$  resonant state. The orange dotted curve illustrates the four-body phase volume  $\approx E_T^{7/2}$  convoluted with the setup bias.

earlier works [3,4,8]. To quantify this fact we performed complete MC simulations for the isolated ground state assuming the  $E_T = 2.6$  MeV resonance energy and angular distribution predicted by calculations of Fig. 7. The MC simulations of

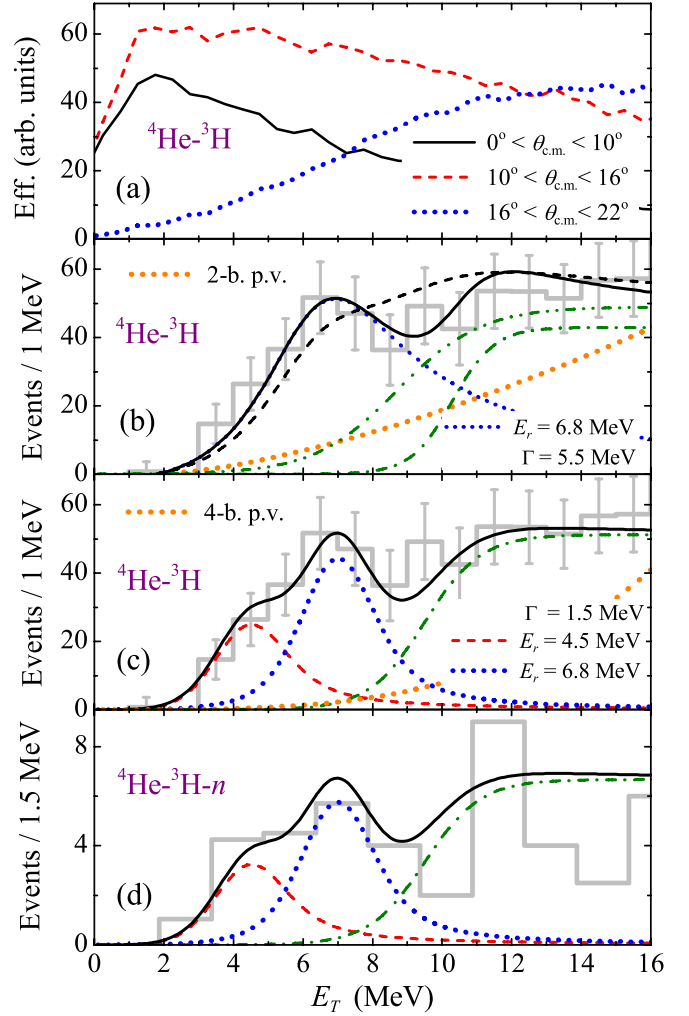


FIG. 12. (a) Efficiency of the  ${}^4\text{He}-{}^3\text{H}$  coincidence registration in different  $\theta_{\text{c.m.}}$  ranges. Possible interpretations of the  ${}^6\text{H}$  spectrum with one broad state (b) or two relatively narrow states (c) and (d). The gray histograms in (b) and (c) show the efficiency-corrected  ${}^4\text{He}-{}^3\text{H}$  coincidence data based on Fig. 10(a). The gray histogram in (d) shows the efficiency-corrected  ${}^4\text{He}-{}^3\text{H}-n$  coincidence data based on Fig. 11(d). The red dashed and blue dotted curves correspond to the possible contributions of the low-energy  ${}^6\text{H}$  states; the green dash-dotted and dash-double-dotted curves are an option for the physical background approximated by the Fermi-type profile. The black solid curves show the sum of all contributions. In panel (b) an alternative fit without an explicit valley at  $E_T \approx 9-10$  MeV is shown by the black dashed curve (the physical background corresponding to it is shown by green dash-double-dotted curve). The two-body phase volume  $\approx (E_T - E_{5\text{H}}^{(R)})^{3/2}$  for the  $p$ -wave  ${}^5\text{H}(\text{g.s.})+n$  channel and the four-body phase volume  $\approx E_T^{7/2}$  and are shown by the orange dotted lines in (b) and (c), respectively.

our setup efficiency—see Fig. 12(a)—show that this energy and angular range  $\theta_{\text{c.m.}} < 16^\circ$  are the most favorable for such a resonant state identification. Figure 13 illustrates which limits on the population of the  $E_T = 2.6$  MeV resonance are imposed by our data. One can see that even without any background subtraction this cross section limit should

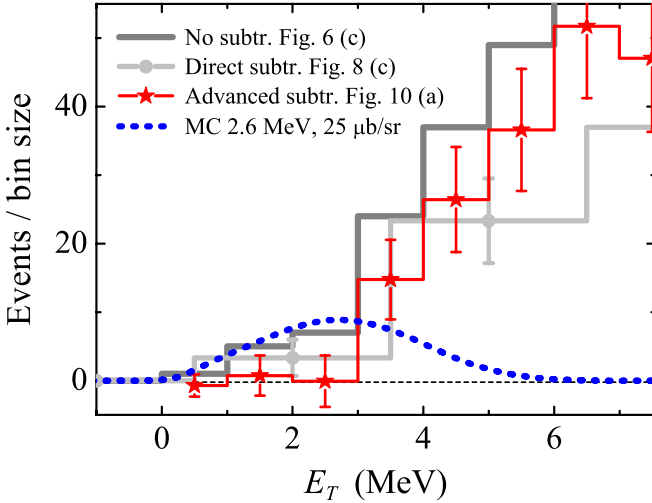


FIG. 13. MC simulations of the possible  ${}^6\text{H}$  g.s. resonance at  $E_T = 2.6$  MeV (blue dotted curve). The gray histogram shows the data without any background subtraction Fig. 6(c). The red and light gray histograms show the results of the direct and advanced empty target background subtractions, see Figs. 8(c) and 10(a), respectively.

be set as  $d\sigma/d\Omega_{c.m.} \lesssim 25 \mu\text{b/sr}$ . Such a value is essentially smaller than  $d\sigma/d\Omega_{c.m.} \approx 190 \mu\text{b/sr}$  both observed around the 6.8 MeV bump and predicted by calculations for  $\Delta l = 1$  angular momentum transfer. It is clear that whatever is the applied background subtraction procedure, the actual cross section limit should be smaller anyhow. With the direct empty target subtraction procedure the cross section limit is obtained as  $d\sigma/d\Omega_{c.m.} \lesssim 12 \mu\text{b/sr}$ ; see Fig. 8(c). According to the advanced subtraction procedure the population is practically zero at  $E_T < 3.5$  MeV; see Fig. 10(a). By assuming that the *three* events, appearing at  $E_T < 3.5$  MeV, could be attributed to such a state, the cross section limit of its population is set as  $d\sigma/d\Omega_{c.m.} \lesssim 5 \mu\text{b/sr}$ .

Here it is natural to ask the question, “What is the lowest resonant energy admissible by our data?” We imply that the population rate for such a state should be comparable for several possible low-lying states of  ${}^6\text{H}$  populated by the  $\Delta l = 1$  angular momentum transfer. It is discussed in the theoretical estimates of Sec. IV that much smaller widths of the low-lying  ${}^6\text{H}$  states are possible than is assumed in Fig. 12(b). For the  $E_T = 6.8$  MeV resonance with a smaller width (e.g.,  $\Gamma = 1.5$  MeV) the interpretation with two states, illustrated in Figs. 12(c) and 12(d), is preferable. The low-energy slope of the cross section can be described by a resonant state with energy as low as  $E_T = 4.5$  MeV. This resonant contribution should be interpreted as the *lowest-energy resonant state* in  ${}^6\text{H}$  with reasonably large population cross section, which can be consistent with our data.

Generally, one should keep in mind that more than two overlapping  ${}^6\text{H}$  states may actually be expected in this energy range. Therefore, the “two-state situation” in reality could mean “more than one state.” The ground state situation of  ${}^6\text{H}$  is further discussed in Sec. V.

#### IV. TRUE AND SEQUENTIAL DECAY OF ${}^6\text{H}$

The simplest idea about the character of the four-body decay is based on the phase volume (p.v.) approximation. The decay mechanism, for which the p.v. approximation is valid, is often discussed as “true four-body decay”: there are no regions in the momentum space which are emphasized by some forms of nuclear dynamics (e.g., strong final state interactions, leading to population of intermediate resonances). The phase space  $dV_4$  of the four-particle system can be defined by the three energies  $E_i = \varepsilon_i E_T$  corresponding to the three Jacobi vectors in momentum space,

$$dV_4 \approx E_T^{9/2} \delta(E_T - \sum_i \varepsilon_i E_T) \sqrt{\varepsilon_1 \varepsilon_2 \varepsilon_3} d\varepsilon_1 d\varepsilon_2 d\varepsilon_3. \quad (1)$$

The one-dimensional phase-volume energy distribution can be obtained by integrating the phase space (1) over the two  $\varepsilon$  variables:

$$dV_4/d\varepsilon \approx E_T^{7/2} \sqrt{\varepsilon(1-\varepsilon)^4}. \quad (2)$$

This expression for the energy distribution is evidently the same for any of the three Jacobi vectors. Therefore, it defines the single-particle energy distributions for both  ${}^3\text{H}$  and  $n$  fragments emitted in the  ${}^6\text{H}$  decay.

A more realistic scenario of the decay of  ${}^6\text{H}$  can be a sequential process: the emission of one neutron, which may lead to the population of the  ${}^5\text{H}$  ground state. For theoretical modeling of the  ${}^6\text{H}$  sequential decay via the  ${}^5\text{H}$  g.s. we employ a generalization of the  $R$ -matrix-type expression, which was previously actively used for the two-nucleon emission estimates in Refs. [16–20]:

$$\begin{aligned} \frac{\Gamma(E_T)}{d\varepsilon_{5\text{H}}} &= \frac{E_T \langle V_3 \rangle^2}{2\pi} \frac{\Gamma_{5\text{H}-n}(E_{5\text{H}-n})}{(E_{5\text{H}-n} - E_{5\text{H}-n}^{(R)})^2 - \Gamma_{5\text{H}-n}^2(E_{5\text{H}-n})/4} \\ &\times \frac{\Gamma_{5\text{H}}(E_{5\text{H}})}{(E_{5\text{H}} - E_{5\text{H}}^{(R)})^2 - \Gamma_{5\text{H}}^2(E_{5\text{H}})/4}, \\ \langle V_3 \rangle^2 &= (E_T - E_{5\text{H}}^{(R)} - E_n^{(R)})^2 \\ &+ [\Gamma_{5\text{H}}(E_{5\text{H}}^{(R)}) + \Gamma_{5\text{H}-n}(E_{5\text{H}-n}^{(R)})]^2 / 4, \\ E_{5\text{H}} &= \varepsilon_{5\text{H}} E_T, \quad E_{5\text{H}-n} = (1 - \varepsilon_{5\text{H}}) E_T, \end{aligned} \quad (3)$$

The  $\Gamma_{5\text{H}}$  width dependence can be parametrized as

$$\Gamma_{5\text{H}}(E_{5\text{H}}) = C_{5\text{H}} E_{5\text{H}}^2, \quad C_{5\text{H}} = 0.5 \text{ MeV}^{-1}. \quad (4)$$

For  $E_{5\text{H}}^{(R)} = 1.8$  MeV this results in  $\Gamma_{5\text{H}} = 1.62$  MeV, which is consistent with the data [9–11]. The neutron width can be defined by the standard  $R$ -matrix expression

$$\Gamma_{5\text{H}-n}(E_{5\text{H}-n}) = 2 \frac{\theta^2}{2M r_c^2} P_{l=1}(E_{5\text{H}-n}, r_c), \quad (5)$$

where  $P_l$  is the penetrability as a function of the decay energy  $E_{5\text{H}-n}$  in the  ${}^5\text{H} + n$  channel and its “channel radius”  $r_c$ . The Lorentz-type profiles used in Eq. (3) for the  ${}^6\text{H}$  estimates are shown in Fig. 14(a). They correspond to the following parameters:  $E_{5\text{H}} = 2.25$  MeV,  $E_{5\text{H}-n}^{(R)} = 8$  MeV,  $r_c = 3$  fm, and  $\theta^2 = 1.5$ . The phase shift in the  ${}^3\text{H} - n$  channel, which can be associated with  $\Gamma_n$  in Eq. (5), is shown in Fig. 14(b): this can be seen as reasonably consistent with phase shifts of

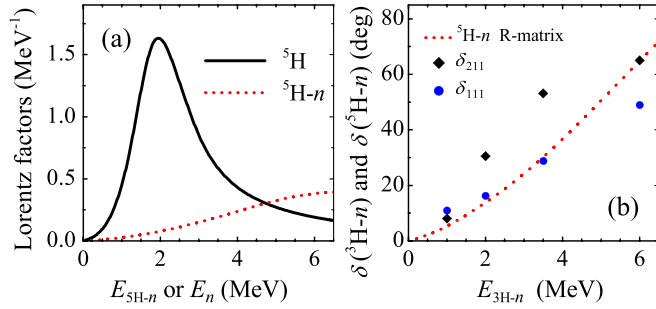


FIG. 14. (a) The Lorentz profiles, as used in Eq. (3), for the  ${}^5\text{H}(\text{g.s.})$  subsystem and for the  ${}^5\text{H}-n$  relative motion. (b) Phase shifts, corresponding to the  ${}^5\text{H}-n$  profile in panel (a), are compared with the experimental phase shifts of the lower spin-doublet states in  ${}^4\text{H}$  with the  $\{j, l, s\}$  sets  $\{1, 1, 1\}$  and  $\{2, 1, 1\}$ .

the lowest states of  ${}^4\text{H}$ . The energy distributions between the  ${}^5\text{H}(\text{g.s.})$  and neutron, calculated by Eq. (3), are illustrated in Fig. 15(b) for two  ${}^6\text{H}$  decay energies.

The  ${}^6\text{H}$  decay width, estimated by Eq. (3), is shown in Fig. 16, together with a trivial estimate of the  $p$ -wave neutron emission on the  ${}^5\text{H}(\text{g.s.})$  threshold made by Eq. (5). For the states with  $E_T = 4.5$  and 6.8 MeV the corresponding width values 3 and 5.5 MeV are obtained. One may see that in proximity of the  ${}^5\text{H}(\text{g.s.})-n$  threshold the width provided by the four-body expression (3) differs qualitatively from that evaluated by (5). At higher energies the difference becomes not so large. The four-body expression provides a result which is somewhat smaller than the two-body one (some part of the  ${}^5\text{H}$  continuum strength described by a broad state remains outside the  ${}^6\text{H}$  decay energy window).

One should also note that the  ${}^6\text{H}$  g.s. may have a quite low spectroscopic factor of the  $n + {}^5\text{H}(\text{g.s.})$  configuration. This idea comes as an analogy with the  ${}^7\text{He}$  g.s. situation, which can also be seen as a hole in the neutron  $p_{3/2}$  subshell from the shell model point of view. The respective neutron spectroscopic factors of 0.3–0.6 are typically derived or predicted for the  ${}^7\text{He}$  g.s. (e.g., [21,22] and references therein). Therefore, the widths provided in Fig. 16 are expected to be the *upper limit estimates* for the widths, and one cannot exclude that the actual widths of the  ${}^6\text{H}$  resonant states are much smaller.

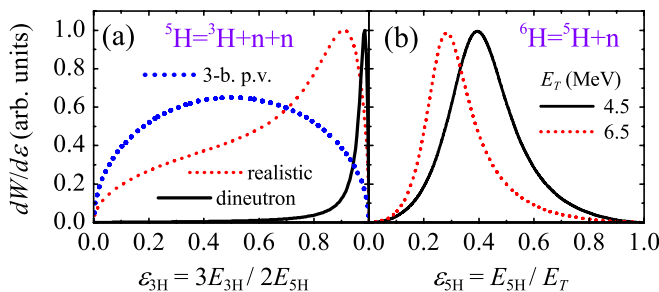


FIG. 15. The  $\varepsilon$  energy distributions. (a) For the  ${}^5\text{H}(\text{g.s.})$  decay, between the  ${}^3\text{H}$  and  $2n$  for different model assumptions about the decay dynamics. (b) For for the  ${}^6\text{H}(\text{g.s.})$  decay, between the  ${}^5\text{H}(\text{g.s.})$  and neutron.

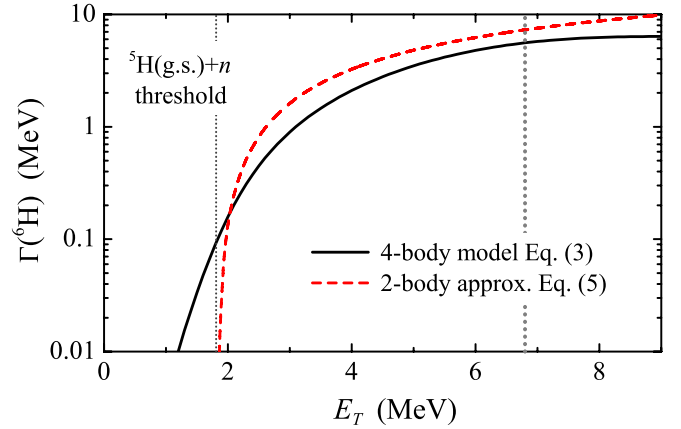


FIG. 16. The  ${}^6\text{H}$  g.s. width as a function of the decay energy estimated by trivial  $R$ -matrix expression (5), assuming two-body decay to the  ${}^5\text{H}(\text{g.s.})$  threshold, and by the four-body sequential model of Eq. (3).

The widths may be around  $\Gamma \approx 1\text{--}3$  MeV, as assumed in Figs. 12(c) and 12(d).

#### A. Energy distributions of the decay products

Though Eq. (3) can be seen as a very simplistic model of the  $3n$  emission in  ${}^6\text{H}$ , it may provide some exclusive information, never considered carefully before: the energy distributions of the decay products of  ${}^6\text{H}$  may be calculated for more complicated dynamical assumptions than phase volume.

For these calculations an additional input is required: the energy distribution  ${}^3\text{H} + n + n$  inside the  ${}^5\text{H}$  subsystem. Here we employ the following three qualitatively different model distributions.

- (i) “3-body p.v.” — three-body phase volume assumption about the decay of the  ${}^5\text{H}$  g.s. (the standard uncorrelated assumption).
- (ii) “realistic” — the  ${}^5\text{H}$  g.s. energy distribution inspired by the experimental data [11].
- (iii) “dineutron” — the highly correlated dineutron decay of the  ${}^5\text{H}$  ground state.

These cases are illustrated in Fig. 15(a). It should be understood what the above mentioned “inspired by experiment” assumption means: the energy distribution for  ${}^5\text{H}$  was reconstructed in [11] in the energy range around the g.s. position (see Figs. 10 and 11 in [11]). However, it is demonstrated in [11] that the contribution of the broad  $5/2^+ - 3/2^+$  doublet of excited  ${}^5\text{H}$  states (located around  $E_T \approx 5$  MeV) is large or even dominant in the  ${}^5\text{H}$  g.s. energy region ( $E_T \approx 1.8$  MeV). For that reason we can only guess or try to predict theoretically [23–25] what is the actual  ${}^5\text{H}$  g.s. decay energy distribution.

By using the inputs from Figs. 14 and 15 we obtain the energy distributions of the neutrons and  ${}^3\text{H}$  fragments in the  ${}^6\text{H}$  rest frame; see Figs. 17 and 18, respectively. The estimated neutron distributions all have a pronounced bimodal shape connected with the assumed sequential  ${}^6\text{H} \rightarrow {}^5\text{H}(\text{g.s.}) + n \rightarrow {}^3\text{H} + 3n$  mechanism of the decay.

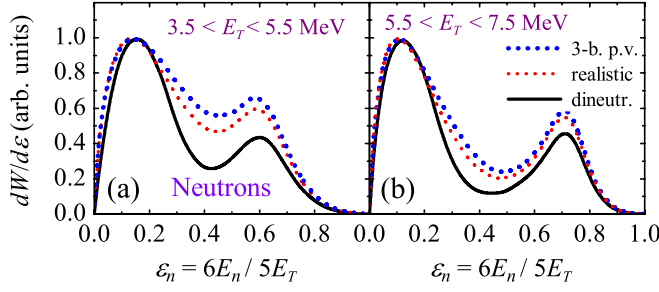


FIG. 17. The calculated  $\varepsilon$  energy distributions of neutrons emitted from the  ${}^6\text{H}$  states at  $E_T = 4.5$  MeV (a) and  $E_T = 6.8$  MeV (b). The black solid, red dashed, and blue dotted curves correspond to the “dineutron,” “realistic,” and three-body phase volume models of the  ${}^5\text{H}$  g.s. decay, respectively.

Unfortunately, the single-neutron distribution is relatively weakly sensitive to the decay mechanism of  ${}^5\text{H}$ , and the energy resolution of the neutron spectrum in Fig. 11 is not sufficient to make practical use of this information. In contrast, the  ${}^3\text{H}$  energy distribution demonstrates strong sensitivity to the correlations in the  ${}^5\text{H}$  intermediate system.

To make the above considerations quantitative, the  ${}^3\text{H}$  energy distributions of Figs. 18(a) and 18(b) were used in MC simulations, which allowed us to take into account the bias of our experimental setup. The resulting distributions are shown in Figs. 18(c) and 18(d), and the numerical information about the  ${}^3\text{H}$  energy distributions is provided in Table II.

The experimental energy distributions for the  ${}^3\text{H}$  fragment in the  ${}^6\text{H}$  c.m. system for the  ${}^4\text{He}-{}^3\text{H}$  and  ${}^4\text{He}-{}^3\text{H}-n$  coincidence events are shown in Figs. 18(e) and 18(f). These distributions are consistent with each other within the available statistics in the energy ranges  $E_T = 3.5\text{--}5.5$  MeV and  $E_T = 5.5\text{--}7.5$  MeV. One may conclude from Fig. 18 and Table II that the preferable interpretation of the data suggests the extremely correlated emission of two neutrons from the  ${}^5\text{H}$ (g.s.) intermediate system.

### V. DISCUSSION

In this section we are going to further argue that the 6.8 MeV bump and cross section rise at 4.5 MeV observed in our work are likely to represent the actual ground state

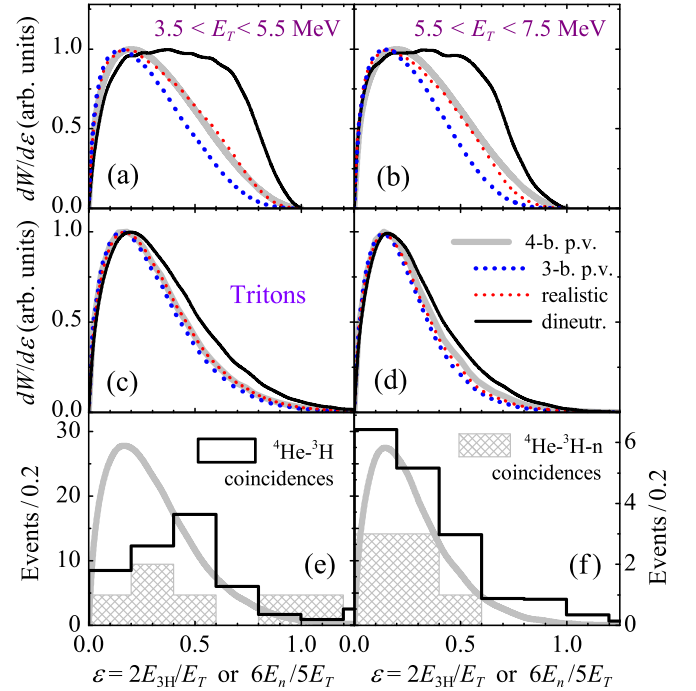


FIG. 18. The  $\varepsilon$  energy distributions of  ${}^3\text{H}$  fragments emitted from the  ${}^6\text{H}$  states at  $E_T = 4.5$  MeV (a,c,e) and  $E_T = 6.8$  MeV (b,d,f). The black solid, red dashed, and blue dotted curves correspond to the “dineutron,” “realistic,” and three-body phase volume models of the  ${}^5\text{H}$  g.s. decay, respectively. The thick gray curve shows the four-body phase volume distribution Eq. (2). Panels (a,b) show the initial theoretical distributions, while in panels (c,d) the experimental setup bias is taken into account via MC procedure. Panels (e,f) show the experimental  $\varepsilon$  energy distributions for the  ${}^3\text{H}$  fragment in the  $E_T$  energy ranges  $\{3.5, 5.5\}$  and  $\{5.5, 7.5\}$  MeV. The black histograms show the distributions obtained from the  ${}^4\text{He}-{}^3\text{H}$  coincidence data (left axis). The gray hatched histograms show the distributions obtained from the  ${}^4\text{He}-{}^3\text{H}-n$  coincidence data (right axis). The MC four-body phase volume distributions are shown by the thick gray curves.

and first excited state (or overlapping lowest excited states). In contrast, the 2.6 MeV ground state, which is broadly accepted now in the literature, has actually very limited experimental support and may be nonexistent.

TABLE II. Mean values of the  $\varepsilon$  distributions of  ${}^3\text{H}$  fragments obtained in the two  $E_T$  decay energy ranges of  ${}^6\text{H}$ . The “th.” columns show the theoretical results and the “bias” columns give the corresponding values corrected for the experimental bias via the MC procedure. The “4-body p.v.” is the four-body phase volume approximation of the true  $3n$  emission from  ${}^6\text{H}$  made by Eq. (2). Models for the sequential  ${}^6\text{H} \rightarrow {}^5\text{H}(\text{g.s.})+n \rightarrow {}^3\text{H}+3n$  decay: “3-body p.v.” — the uncorrelated three-body phase volume decay of the  ${}^5\text{H}$  g.s.; “realistic” — the experiment-inspired distribution for the  ${}^5\text{H}$  g.s.; “dineutron” — the highly correlated dineutron decay of the  ${}^5\text{H}$  ground state. The column “experiment” shows the data from Figs. 11 and 18. The experimental errors are calculated by the MC procedure based on the available experimental statistics in each case.

| Range (MeV)       | 4-body p.v. |      | 3-body p.v. |      | realistic |      | dineutron |      | experiment                   |                                |
|-------------------|-------------|------|-------------|------|-----------|------|-----------|------|------------------------------|--------------------------------|
|                   | th.         | bias | th.         | bias | th.       | bias | th.       | bias | ${}^4\text{He}-{}^3\text{H}$ | ${}^4\text{He}-{}^3\text{H}-n$ |
| $3.5 < E_T < 5.5$ | 1/3         | 0.30 | 0.29        | 0.28 | 0.33      | 0.30 | 0.43      | 0.39 | 0.42(3)                      | 0.49(7)                        |
| $5.5 < E_T < 7.5$ | 1/3         | 0.28 | 0.27        | 0.24 | 0.31      | 0.26 | 0.39      | 0.33 | 0.33(2)                      | 0.24(8)                        |

### A. Does the 2.6 MeV state exist in the ${}^6\text{H}$ ?

The vision that the 2.6 MeV ground state energy of  ${}^6\text{H}$  is solidly established is quite widespread. We have to point here that this misleading impression is partly supported by some problems of data *representation* in the NNDC database. Namely, in NNDC page for the  ${}^6\text{H}$  level scheme one gets information that the ground state population was taking place in *all the five* available reactions: three in papers [3,4,8] and two in [7]. Such a broad experimental support may look impressive. However, if one opens the corresponding evaluation files from NNDC [15] for the  ${}^6\text{H}$  population in pion absorption reactions “B” and “D” (based on Ref. [7]), then it is easy to find out that the presumed  ${}^6\text{H}$  g.s. at 2.6 MeV is actually not populated in these reactions. The lowest-energy state, as obtained in this work, has energies 6.6(7) MeV for the  ${}^9\text{Be}(\pi^-, pd){}^6\text{H}$  reaction and 7.3(10) MeV for the  ${}^{11}\text{B}(\pi^-, p^4\text{He}){}^6\text{H}$  reaction. These values are evidently in a nice agreement with our 6.8(5) MeV bump.

The spectra shown in Ref. [7] have good statistics (thousands of events), comparable to statistics obtained in our experiment. The shapes of the MM spectra are qualitatively the same as our MM spectrum: the energy region under  $E_T \approx 3$  MeV is poorly populated; then, there is a kink or bump in the spectra at about  $E_T \approx 7$  MeV; at higher energy the spectrum is reasonably flat. Actually, two reasonably consistent sets of excited states are additionally claimed in Ref. [7]:  $E_T = \{10.7(7), 15.3(7), 21.3(4)\}$  MeV, populated in the  ${}^9\text{Be}(\pi^-, pd){}^6\text{H}$  reaction, and  $E_T = \{14.5(10), 21.3(4)\}$  MeV states populated in the  ${}^{11}\text{B}(\pi^-, p^4\text{He}){}^6\text{H}$  reaction. We observe some oscillation in this energy range in our spectrum with statistical significance analogous to that of Ref. [7]; however, we consider this statistical significance as insufficient to claim additional states in the spectrum of  ${}^6\text{H}$ .

The studies of the  ${}^6\text{Li}(\pi^-, \pi^+){}^6\text{H}$  reaction provided no evidence for low-lying resonant states of  ${}^6\text{H}$  [5,6]. The authors performed a dedicated search for the 2.6 MeV ground state and found that “In the missing mass region 0–5 MeV 95% confidence upper limits of 0–5 nb/sr for the production cross section were set.” This limit should be compared to the typical expected  ${}^6\text{H}$  g.s. population cross section of  $\approx 40$  nb/sr for this reaction. If we look directly at the missing mass spectrum of the  ${}^6\text{Li}(\pi^-, \pi^+){}^6\text{H}$  reaction in [5], then some evidence for a kink in the spectrum can be seen at  $E_T \approx 7$ –9 MeV, where the typical resonant population cross section of  $\approx 30$ –70 nb/sr is achieved. So, these data can be seen as being in qualitative agreement with our result: there is no expressed bump in the cross section, but the typical resonant cross section is achieved at energies consistent with our  $E_T \approx 6.8$  MeV value.

We now give a critical review of the experiments in which the 2.6 MeV g.s. was observed.

The  ${}^6\text{H}$  resonant state was reported for the first time in Ref. [3]. It gives the g.s. energy  $E_T = 2.7(4)$  MeV for the  ${}^6\text{H}$  state produced in the  ${}^7\text{Li}({}^7\text{Li}, {}^8\text{B}){}^6\text{H}$  reaction. Actually a broad structure with  $E_T = 1.8$ –4.5 MeV is observed, which statistically is quite convincing ( $\approx 300$  events). The data are strongly contaminated with various backgrounds

(40–60% in the region of the resonance bump, according to [3]). The mechanism of this reaction is a complicated “bidirectional” transfer ( $-2p, +1n$ ). Now we can point that  ${}^7\text{Li}({}^7\text{Li}, {}^9\text{B}^*){}^5\text{H}(\text{g.s.})$  can be responsible for the formation of this bump, where the  ${}^9\text{B}^*$  excited states located somewhat above the  ${}^8\text{B}+n$  threshold are populated (for example, the  $E^* = 18.6$  or 20.7 MeV states). This is the much “easier” reaction (just  $-2p$  transfer) and something like an order of the magnitude higher population cross section may be expected for it. The authors of [3] avoided this interpretation, as “the  ${}^5\text{H}$  nucleus is known not to exist.” Now the low-lying resonant g.s. of  ${}^5\text{H}$  with  $E_T \approx 1.8$  MeV is solidly established and its population seem to be very favourable scenario for this reaction.

The  $E_T = 2.6(5)$  MeV bump was claimed to be observed in the  ${}^9\text{Be}({}^{11}\text{B}, {}^{14}\text{O}){}^6\text{H}$  reaction in Ref. [4]. There are problematic issues concerning this experiment. (i) It has marginal statistics and large backgrounds ( $\approx 20$  events are spread on the top of  $\approx 40$  of expected background events). (ii) The obtained events are actually spread in a much narrower energy range  $E_T = 2.1$ –3.1 MeV than in [3]. Point (ii) is probably partly connected with fact that the kinematical cutoff for the  ${}^9\text{Be}({}^{11}\text{B}, {}^{14}\text{O}){}^6\text{H}$  reaction in [4] is taking place at  $E_T \approx 3.2$ –3.5 MeV leading to unknown strong distortions of the MM spectrum in the region of the expected  ${}^6\text{H}$  resonance peak. (iii) The ground state of the neighboring  ${}^5\text{H}$  nuclide was not observed in Ref. [4] in the analogous  ${}^9\text{Be}({}^{11}\text{B}, {}^{15}\text{O}){}^5\text{H}$  reaction (otherwise providing on average a reliable tenfold larger statistics than  ${}^6\text{H}$  data).

The  ${}^6\text{H}$  g.s. energy of  $E_T = 2.9(9)$  MeV was claimed in [8] based on events which could originate from the  ${}^8\text{He}({}^{12}\text{C}, {}^{14}\text{N}){}^6\text{H}$  reaction. The problem is that there was no channel identification in [8] which can reliably distinguish among the  ${}^{13}\text{N}$ ,  ${}^{14}\text{N}$ , and  ${}^{15}\text{N}$  recoils, and, consequently, among the  ${}^7\text{H}$ ,  ${}^6\text{H}$ , and  ${}^5\text{H}$  products. Assignment for each of these products was solely based on assumption that only the low-lying near-threshold ground state is populated in each case. Specifically for  ${}^6\text{H}$  in [8] there are *five* events spread from 0 to 7.5 MeV excitation in the MM spectrum and only *three* events located between 1.5 to 5.5 MeV were assigned as belonging to the  ${}^6\text{H}$  g.s. resonance. This kind of data, taken without interpretation, actually can be considered as not contradicting our data.

So, we can see that the  $E_T \approx 2.6$  MeV state has very questionable support in experimental data. All the experiments [3,4,8] in which it was observed have important experimental problems (statistical significance, channel identification, etc.). In contrast, in experiments with large statistics, clear channel identification and background treatment (Refs. [5,7] and our data) one gets the first expressed lowest-energy feature at  $E_T \approx 7$  MeV. It is, of course, not impossible, that the  $\approx 2.6$  MeV state was specifically poorly populated in the reactions of Ref. [5,7] and our reaction. However, this suggestion is quite implausible, as there should be several excited states of  ${}^6\text{H}$  (all populated by the same  $\Delta l = 1$  as the ground state) within several MeV of excitation. All of them are expected to be populated comparably with the ground state. Here we find the 6.8 MeV bump, having a cross section typical for a direct single-step transfer reaction (e.g.,  $d\sigma/d\Omega_{\text{c.m.}} \approx 190 \mu\text{b/sr}$  in

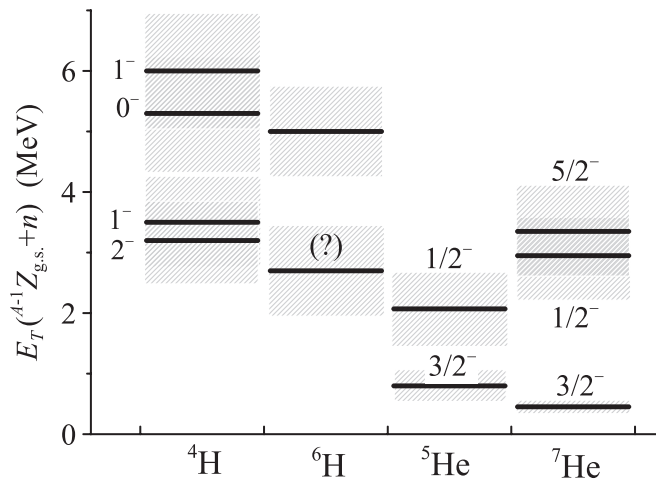


FIG. 19. Evolution of the level scheme of the  ${}^5\text{He}$ - ${}^4\text{H}$  pair (one neutron particle in the  $p_{3/2}$  subshell) and the  ${}^7\text{He}$ - ${}^6\text{H}$  pair (one neutron hole in the  $p_{3/2}$  subshell). The energies are calculated relative to the one-neutron separation threshold (the  ${}^5\text{H}$  g.s. is assumed to be 1.8 MeV above the two-neutron separation threshold [9,11]).

our reaction), while for the  $\approx 2.6$  MeV energy region quite a reliable population limit  $d\sigma/d\Omega_{\text{c.m.}} \lesssim 5 \mu\text{b/sr}$  is established.

We suggest considering the location of the  ${}^6\text{H}$  g.s. as an open question and provide below some theoretical arguments supporting the g.s. prescription based on the data of our work.

### B. Analogies among He and H excitation spectra

Let us consider the energy level evolution from  ${}^5\text{He}$  (with the assumed configuration of one neutron particle in the  $p_{3/2}$  subshell) to  ${}^7\text{He}$  (one neutron hole in the  $p_{3/2}$  subshell); see Fig. 19. The  $3/2^-$  ground state of  ${}^7\text{He}$  becomes more bound than that in  ${}^5\text{He}$ . The experimental status of the  $1/2^-$  state in  ${}^7\text{He}$  is not well established (see, e.g., [21]); however, it seems to have higher excitation energy than the  $1/2^-$  state in  ${}^5\text{He}$ . Moreover, it is highly likely that there is a  $5/2^-$  state in  ${}^7\text{He}$ , built on the  $2^+$  excitation of  ${}^6\text{He}$  [26,27], which, evidently, has no counterpart in  ${}^5\text{He}$ .

If we consider evolution from  ${}^5\text{He}$  to  ${}^4\text{H}$ , then the  $\{3/2^-, 1/2^-\}$  spin-orbit doublet is replaced by a quadruplet  $\{2^-, 1^-, 1^-, 0^-\}$  of states due to splitting induced by the  ${}^3\text{H}$  spin. If we extend the  ${}^5\text{He}$ - ${}^7\text{He}$  analogy of Fig. 19 to the  ${}^6\text{H}$  states, then two effects are expected.

(i) Following the  ${}^7\text{He}$  vs  ${}^5\text{He}$  analogy, we expect that the  ${}^6\text{H}$  g.s. is more bound than the  ${}^4\text{H}$  ground state. This assumption is true if the 4.5 MeV state really exists in  ${}^6\text{H}$ .

(ii) In the range  $4 < E_T < 9$  MeV we expect *six* states of  ${}^6\text{H}$ . So, it is highly likely that the broad 6.8 MeV structure is actually a superposition of several overlapping states, which are populated in unknown proportions and could not be resolved in the inclusive (no correlation) experiment. It still makes sense to distinguish the 4.5 MeV state as the lowest energy resonance, which is allowed by our data, and thus is a candidate to represent the  ${}^6\text{H}$  ground state.

### C. Pairing energy

As we mentioned in the Introduction, the  ${}^6\text{H}$  g.s. position was suggested to be at  $E_T = 2.6$ – $2.9$  MeV in Refs. [3,4,8]. However, now the g.s. energies are known for  ${}^5\text{H}$  ( $E_T \approx 1.8$  MeV [9,11]; the  $E_T = 2.4(3)$  MeV value from [28] is practically consistent with this value) and  ${}^7\text{H}$  ( $E_T \approx 2.2$  MeV [2]; we regard the  $E_T \approx 0.3 - 1$  MeV value from [8] as much less reliable). Based on these values, the energy reported in [3,4,8] for the  ${}^6\text{H}$  ground state would mean the lack of the neutron pairing effect in the even-neutron nucleus  ${}^7\text{H}$  (experimental pairing energy appears to be  $\approx 0.7$ – $1$  MeV compared with  $\approx 3$  MeV expected in analogy with the  ${}^7\text{He}$ - ${}^8\text{He}$  pair). Hence, we conclude that the results reported in Refs. [3,4,8] are not compatible with the standard pairing assumption. The  ${}^6\text{H}$  ground state suggested in this work at  $E_T = 4.5$  MeV precisely fits the pairing energy systematics.

### D. Strong $nn$ correlation observed in pion double charge exchange

The search for  ${}^6\text{H}$  in the  ${}^6\text{Li}(\pi^-, \pi^+)$  reaction provided no g.s. identification in the  $E_T = 0$ – $5$  MeV range [5]. However, the authors pointed in a dedicated paper [6] that the peculiar behavior of the low-energy  ${}^6\text{H}$  missing mass spectrum can be understood as being connected with the presence of a strongly correlated  $2n$  configuration in the  ${}^6\text{H}$  continuum considered as  ${}^3\text{H} + n + 2n$ . We should emphasize that this observation is actually consistent with the observation of the strong  $n$ - $n$  correlation in the  ${}^6\text{H}$  decay made in this work, and in  ${}^5\text{H}$  decay in Ref. [11].

## VI. CONCLUSIONS

The  ${}^6\text{H}$  spectrum was populated in this work in the  ${}^2\text{H}({}^8\text{He}, {}^4\text{He}){}^6\text{H}$  transfer reaction. The broad bump in the  ${}^6\text{H}$  MM spectrum at  $E_T = 4$ – $8$  MeV is reliably identified in the data with the population cross section  $d\sigma/d\Omega_{\text{c.m.}} \approx 190_{-80}^{+40} \mu\text{b/sr}$  in the  $5^\circ < \theta_{\text{c.m.}} < 16^\circ$  angular range. This is a reasonably large cross section, consistent with the resonant population mechanism. This bump can be interpreted as a broad ( $\Gamma > 5$  MeV) resonant state at  $E_T = 6.8(5)$  MeV. Actually this could be either a single state or a set of broad overlapping  $p$ -wave states, as expected from analogy with the known  ${}^4\text{H}$  spectrum. Observation of such a state (or states) is consistent with the data of Ref. [7], concerning the lowest  ${}^6\text{H}$  state.

We have found *no evidence* of the  $\approx 2.6$ – $2.9$  MeV state in  ${}^6\text{H}$ , which was reported in the pioneering work [3] and has support in [4,8]. The cross section limit  $d\sigma/d\Omega_{\text{c.m.}} \lesssim 5 \mu\text{b/sr}$  is set for the population of possible states with  $E_T < 3.5$  MeV. Also the existence of the  ${}^6\text{H}$  g.s. at  $\approx 2.6$ – $2.9$  MeV is hardly consistent, due to the pairing energy argument, with the observation of the  ${}^7\text{H}$  g.s. at  $2.2(5)$  MeV [2]. There is no sensible structural argument explaining why the population of the possible  $\approx 2.6$ – $2.9$  MeV ground state could be suppressed in a very “simplistic”  ${}^2\text{H}({}^8\text{He}, {}^4\text{He}){}^6\text{H}$  transfer reaction and not observed in our data, while the  ${}^6\text{H}$  spectrum at  $E_T \gtrsim 3.5$  MeV is well populated. Therefore, we suggest that the

position of the  ${}^6\text{H}$  g.s. is not yet established, and discussion of this issue should be continued.

The broad bump in the  ${}^6\text{H}$  MM spectrum at  $E_T = 4\text{--}8$  MeV can also be interpreted as overlap of two relatively narrow states. Such an interpretation of the experimental spectrum allows us to establish  $E_T = 4.5(3)$  MeV as the *low-energy limit* for the  ${}^6\text{H}$  ground state energy admissible by our data. According to the energy systematics and the pairing energy arguments, resonance with such an energy is a good candidate for the  ${}^6\text{H}$  ground state.

The low-energy limit of the  ${}^6\text{H}$  g.s. position, established as  $E_T = 4.5(3)$  MeV, confirms that the decay mechanism of the  ${}^7\text{H}$  g.s. (located at 2.2 MeV above the  ${}^3\text{H} + 4n$  threshold [2]) is the “true” (or simultaneous)  $4n$  emission. Thus, the  ${}^7\text{H}$  is the first confirmed case of a nucleus possessing this exclusive few-body dynamics of decay.

The momentum distribution of the  ${}^3\text{H}$  decay fragments was reconstructed in the  ${}^6\text{H}$  rest frame. In this work theoretical studies of the four-body sequential  ${}^6\text{H} \rightarrow {}^5\text{H}(\text{g.s.}) + n \rightarrow {}^3\text{H} + 3n$  decays were performed for the first time. Within the assumption of the  ${}^6\text{H}$  sequential decay we have found that our data provide evidence that an extremely strong “dineutron-

type” correlation is realized in the decay of the  ${}^5\text{H}$  ground state. More accurate measurements are needed for more solid conclusions. However, a potentially powerful approach for extracting information about the nuclear decay dynamics is already illustrated in our work.

It is clear that our work paves a way to more detailed studies of the  ${}^2\text{H}({}^8\text{He}, {}^4\text{He}){}^6\text{H}$  reaction, which would be able to provide unequivocal results on the excitation spectrum of  ${}^6\text{H}$ .

#### ACKNOWLEDGMENTS

This work was partly supported by the Russian Science Foundation Grant No. 22-12-00054. I.A.M. was supported by the Student Grant Foundation of the Silesian University in Opava, Grant No. SGF/2/2020, which was realized within the EU OPSRE project entitled “Improving the quality of the internal grant scheme of the Silesian University in Opava,” No. CZ.02.2.69/0.0/0.0/19\_073/00116951. The authors are grateful to Prof. M. S. Golovkov for help in the work and useful remarks. We acknowledge the interest and support of this activity from Profs. Yu. Ts. Oganessian and S. N. Dmitriev.

- 
- [1] A. A. Bezbakh, V. Chudoba, S. A. Krupko, S. G. Belogurov, D. Biare, A. S. Fomichev, E. M. Gazeeva, A. V. Gorshkov, L. V. Grigorenko, G. Kaminski, O. A. Kiselev, D. A. Kostyleva, M. Y. Kozlov, B. Mauey, I. Mukha, I. A. Muzalevskii, E. Y. Nikolskii, Y. L. Parfenova, W. Piatek, A. M. Quynh *et al.*, *Phys. Rev. Lett.* **124**, 022502 (2020).
- [2] I. A. Muzalevskii, A. A. Bezbakh, E. Y. Nikolskii, V. Chudoba, S. A. Krupko, S. G. Belogurov, D. Biare, A. S. Fomichev, E. M. Gazeeva, A. V. Gorshkov, L. V. Grigorenko, G. Kaminski, O. Kiselev, D. A. Kostyleva, M. Y. Kozlov, B. Mauey, I. Mukha, Y. L. Parfenova, W. Piatek, A. M. Quynh *et al.*, *Phys. Rev. C* **103**, 044313 (2021).
- [3] D. V. Aleksandrov, E. A. Ganza, Yu. A. Glukhov, B. G. Novatsky, A. A. Ogloblin, and D. N. Stepanov, *Yad. Fiz.* **39**, 513 (1984).
- [4] A. Belozorov, C. Borcea, Z. Dlouhy, A. Kalinin, R. Kalpakchieva, N. H. Chau, Y. Oganessian, and Y. Penionzhkevich, *Nucl. Phys. A* **460**, 352 (1986).
- [5] B. Parker, K. K. Seth, and R. Soundranayagam, *Phys. Lett. B* **251**, 483 (1990).
- [6] K. K. Seth and B. Parker, *Phys. Rev. Lett.* **66**, 2448 (1991).
- [7] Y. Gurov, B. Chernyshev, S. Isakov, V. S. Karpukhin, S. Lapushkin, I. V. Laukhin, V. A. Pechkurov, N. O. Poroshin, and V. Sandukovsky, *Eur. Phys. J. A* **32**, 261 (2007).
- [8] M. Caamaño, D. Cortina-Gil, W. Mittig, H. Savajols, M. Chartier, C. E. Demonchy, B. Fernández, M. B. G. Hornillos, A. Gillibert, B. Jurado, O. Kiselev, R. Lemmon, A. Obertelli, F. Rejmund, M. Rejmund, P. Roussel-Chomaz, and R. Wolski, *Phys. Rev. C* **78**, 044001 (2008).
- [9] A. A. Korshennikov, M. S. Golovkov, I. Tanihata, A. M. Rodin, A. S. Fomichev, S. I. Sidorchuk, S. V. Stepantsov, M. L. Chelnokov, V. A. Gorshkov, D. D. Bogdanov, R. Wolski, G. M. Ter-Akopian, Y. T. Oganessian, W. Mittig, P. Roussel-Chomaz, H. Savajols, E. A. Kuzmin, E. Y. Nikolskii, and A. A. Ogloblin, *Phys. Rev. Lett.* **87**, 092501 (2001).
- [10] M. S. Golovkov, L. V. Grigorenko, A. S. Fomichev, S. A. Krupko, Y. T. Oganessian, A. M. Rodin, S. I. Sidorchuk, R. S. Slepnev, S. V. Stepantsov, G. M. Ter-Akopian, R. Wolski, M. G. Itkis, A. A. Bogatchev, N. A. Kondratiev, E. M. Kozulin, A. A. Korshennikov, E. Y. Nikolskii, P. Roussel-Chomaz, W. Mittig, R. Palit *et al.*, *Phys. Rev. Lett.* **93**, 262501 (2004).
- [11] M. S. Golovkov, L. V. Grigorenko, A. S. Fomichev, S. A. Krupko, Y. T. Oganessian, A. M. Rodin, S. I. Sidorchuk, R. S. Slepnev, S. V. Stepantsov, G. M. Ter-Akopian, R. Wolski, M. G. Itkis, A. S. Denikin, A. A. Bogatchev, N. A. Kondratiev, E. M. Kozulin, A. A. Korshennikov, E. Y. Nikolskii, P. Roussel-Chomaz, W. Mittig *et al.*, *Phys. Rev. C* **72**, 064612 (2005).
- [12] A. S. Fomichev, L. V. Grigorenko, S. A. Krupko, S. V. Stepantsov, and G. M. Ter-Akopian, *Eur. Phys. J. A* **54**, 97 (2018).
- [13] G. Kaminski, B. Zalewski, S. Belogurov, A. Bezbakh, D. Biare, V. Chudoba, A. Fomichev, E. Gazeeva, M. Golovkov, A. Gorshkov, L. Grigorenko, D. Kostyleva, S. Krupko, I. Muzalevsky, E. Nikolskii, Y. Parfenova, P. Plucinski, A. Quynh, A. Serikov, S. Sidorchuk *et al.*, *Nucl. Instrum. Methods Phys. Res., Sect. B* **463**, 504 (2020).
- [14] A. A. Bezbakh, S. G. Belogurov, R. Wolski, E. M. Gazeeva, M. S. Golovkov, A. V. Gorshkov, G. Kaminski, M. Y. Kozlov, S. A. Krupko, I. A. Muzalevsky, E. Y. Nikolskii, E. V. Ovcharenko, R. S. Slepnev, G. M. Ter-Akopian, A. S. Fomichev, P. G. S. V. Chudoba, and V. N. Schetinina, *Instrum. Exp. Tech.* **61**, 631 (2018).
- [15] NNDC database: <http://www.nndc.bnl.gov/>.
- [16] L. V. Grigorenko and M. V. Zhukov, *Phys. Rev. C* **76**, 014009 (2007).
- [17] L. V. Grigorenko, T. D. Wisner, K. Mercurio, R. J. Charity, R. Shane, L. G. Sobotka, J. M. Elson, A. H. Wuosmaa, A. Banu, M. McCleskey, L. Trache, R. E. Tribble, and M. V. Zhukov, *Phys. Rev. C* **80**, 034602 (2009).

- [18] E. Olsen, M. Pfützner, N. Birge, M. Brown, W. Nazarewicz, and A. Perhac, *Phys. Rev. Lett.* **110**, 222501 (2013).
- [19] K. W. Brown, R. J. Charity, L. G. Sobotka, L. V. Grigorenko, T. A. Golubkova, S. Bedoor, W. W. Buhro, Z. Chajeccki, J. M. Elson, W. G. Lynch, J. Manfredi, D. G. McNeel, W. Reviol, R. Shane, R. H. Showalter, M. B. Tsang, J. R. Winkelbauer, and A. H. Wuosmaa, *Phys. Rev. C* **92**, 034329 (2015).
- [20] L. V. Grigorenko and M. V. Zhukov, *Phys. Rev. C* **91**, 064617 (2015).
- [21] F. Renzi, R. Raabe, G. Randisi, D. Smirnov, C. Angulo, J. Cabrera, E. Casarejos, T. Keutgen, A. Ninane, J. L. Charvet, A. Gillibert, V. Lapoux, L. Nalpas, A. Obertelli, F. Skaza, J. L. Sida, N. A. Orr, S. I. Sidorchuk, R. Wolski, M. J. G. Borge *et al.*, *Phys. Rev. C* **94**, 024619 (2016).
- [22] H. T. Fortune, *Eur. Phys. J. A* **54**, 51 (2018).
- [23] N. B. Shul'gina, B. V. Danilin, L. V. Grigorenko, M. V. Zhukov, and J. M. Bang, *Phys. Rev. C* **62**, 014312 (2000).
- [24] L. V. Grigorenko, N. K. Timofeyuk, and M. V. Zhukov, *Eur. Phys. J. A* **19**, 187 (2004).
- [25] L. V. Grigorenko, *Eur. Phys. J. A* **20**, 419 (2004).
- [26] A. A. Korshennikov, M. S. Golovkov, A. Ozawa, E. A. Kuzmin, E. Y. Nikolskii, K. Yoshida, B. G. Novatskii, A. A. Ogloblin, I. Tanihata, Z. Fulop, K. Kusaka, K. Morimoto, H. Otsu, H. Petruscu, and F. Tokanai, *Phys. Rev. Lett.* **82**, 3581 (1999).
- [27] A. H. Wuosmaa, J. P. Schiffer, K. E. Rehm, J. P. Greene, D. J. Henderson, R. V. F. Janssens, C. L. Jiang, L. Jisonna, J. C. Lighthall, S. T. Marley, E. F. Moore, R. C. Pardo, N. Patel, M. Paul, D. Peterson, S. C. Pieper, G. Savard, R. E. Segel, R. H. Siemssen, X. D. Tang, and R. B. Wiringa, *Phys. Rev. C* **78**, 041302(R) (2008).
- [28] A. H. Wuosmaa, S. Bedoor, K. W. Brown, W. W. Buhro, Z. Chajeccki, R. J. Charity, W. G. Lynch, J. Manfredi, S. T. Marley, D. G. McNeel, A. S. Newton, D. V. Shetty, R. H. Showalter, L. G. Sobotka, M. B. Tsang, J. R. Winkelbauer, and R. B. Wiringa, *Phys. Rev. C* **95**, 014310 (2017).